学位論文

Doctor's Thesis

Usefulness of diffusion-weighted MR imaging for the diagnosis of neoplasms

(腫瘍におけるMR拡散強調画像の有用性)

林田　佳子

Yoshiko Hayashida

熊本大学院医学研究科博士課程内科系専攻放射線医学

指導：　山下　康行教授

2006年 3月

学位論文

Doctor's Thesis

Usefulness of diffusion-weighted MR imaging for the diagnosis of neoplasms

（腫瘍における MR 拡散強調画像の有用性）

著者名　　林田　佳子　Yoshiko Hayashida

指導教員名　山下　康行　教授

審査委員名　放射線治療医学担当教授　大屋夏生

細胞病理学担当教授　竹屋元裕

循環器病態学担当教授　小川久雄

形態構築学担当教授　児玉公道

2006 年 3 月

Contents

Summary

Diffusion-weighted MR imaging (DWI) visualizes the random microscopic motion of molecules and thereby provides a tissue contrast different from T1 and T2 in the examined tissues. Diffusion can be quantitatively evaluated by the apparent diffusion coefficients (ADCs), which is independent from proton density, T1, and T2 relaxation effects. Such sequences have been mostly used for the diagnosis of early stroke, but applications in other fields such as oncological and musculoskeletal imaging are being explored.

The high sensitivity and specificity of DWI in the diagnosis of acute cerebral infarction is widely accepted. The reduced diffusion typical of acute stroke is thought to be related to the cytotoxic edema and shrinking of the extracellular space. From this evidence, we can hypothesize that DWI may enable us to differentiate various tumor components and tumoral pathological differentiations.

The purposes of our study were as follows: 1) to compare the capability of conventional MR imaging and diffusion-weighted imaging to delineate components of metastatic brain tumor; 2) to evaluate the usefulness of DWI for the differential diagnosis of poorly contrast-enhanced and T2-prolonged bone masses 3) to evaluate the usefulness of DWI of monitoring response of the therapy in musculoskeletal sarcomas confirmed by histology and 4) to find correlations (1-3) if any, between ADC values and histologic analysis of tumors.

Publication lists

○ 1 **Hayashida Y,** Hirai T,Katahira T, Yamashita Y

Evaluation of diffusion-weighted imaging for the differential diagnosis of poorly contrast-enhanced and T2-prolonged bone masses: initial experience. JMRI 2006 in press

○ 2. **Hayashida Y,** Hirai T, Kitajima M, Yamashita Y

Diffusion-weighted Imaging of Metastatic Brain Tumors: Comparison with Histologic Type and Tumor Cellularity

AJNR Am J Neuroradiol. August 2006, in press.

○ 3. **Hayashida Y,** Yakusiji T, Awai K, Yamashita Y, Mizuta T.

Monitoring response of the therapy in musculoskeletal tumors

Usefulness of Diffusion weighted imaging

European radiology ; in submission

4. Hirai T, Ando Y, Yamura M, Kitajima M, **Hayashida Y,** Korogi Y, Yamashita T, Yamashita Y.

Transthyretin-related familial amyloid polyneuropathy: evaluation of CSF enhancement on serial T1-weighted and fluid-attenuated inversion recovery images following intravenous contrast administration. AJNR Am J Neuroradiol. 2005 Sep;26(8):2043-8.

5. Kitajima M, Hirai T, Korogi Y, Yamura M, Kawanaka K, Ikushima I, **Hayashida Y,** Yamashita Y, Kuratsu J.

Retrograde cortical and deep venous drainage in patients with intracranial dural arteriovenous fistulas: comparison of MR imaging and angiographic findings. AJNR Am J Neuroradiol. 2005 Jun-Jul;26(6):1532-8.

6. Yamura M, Hirai T, Korogi Y, Kitajima M, **Hayashida Y,** Ikushima I, Endo F, Yamashita Y. Evaluation of small hypothalamic hamartomas with 3D constructive interference in steady state (CISS) sequence.

Neuroradiology. 2005 Mar;47(1):204-8. Epub 2005 Feb 25.

7. Kitajima M, Korogi Y, Yamura M, Ikushima I, **Hayashida Y,** Ando Y, Uchino M, Yamashita Y. Familial amyloid polyneuropathy: hypertrophy of ligaments supporting the spinal cord. AJNR Am J Neuroradiol. 2004 Oct;25(9):1599-602.

8 **Hayashida Y,** Hirai T, Korogi Y, Kochi M, Maruyama N, Yamura M, Yamashita Y. Pineal cystic germinoma with syncytiotrophoblastic giant cells mimicking MR imaging findings of a pineal cyst. AJNR Am J Neuroradiol. 2004 Oct;25(9):1538-40.

9 Morishita S, Honda S, Awai K, Hatanaka Y, **Hayashida Y,** Imuta M, Yamashita Y. Role of preoperative helical CT before laparoscopic cholecystectomy: evaluation of gallbladder and peritoneal adhesion.
Radiat Med. 2004 Mar-Apr;22(2):111-5.

10 Utsunomiya D, Notsute S, **Hayashida Y,** Lwakatare F, Katabuchi H, Okamura H, Awai K, Yamashita Y. Endometrial carcinoma in adenomyosis: assessment of myometrial invasion on T2-weighted spin-echo and gadolinium-enhanced T1-weighted images.
AJR Am J Roentgenol. 2004 Feb;182(2):399-404.

11 Nakayama Y, Imuta M, Funama Y, Kadota M, Utsunomiya D, Shiraishi S, **Hayashida Y,** Yamashita Y.
CT portography by multidetector helical CT: comparison of three rendering models. Radiat Med. 2002 Nov-Dec;20(6):273-9.

12 Miyazaki T, Saitoh R, Doi T, **Hayashida Y,** Seishi I, Takahashi M.
Embolization of a pseudoaneurysm in the transplanted kidney.
AJR Am J Roentgenol. 1998 Dec;171(6):1617-8.

Acknowledgements

These academic investigations were done during my post graduate period from 2001 to 2005 at department of Diagnostic Radiology Graduate School of Medical Sciences, Kumamoto University.

I wish to extend my sincere thanks to Professor Yasuyuki Yamashita, Chairman of the department of Diagnostic Radiology Graduate School of Medical Sciences, Kumamoto University for general guidance and constructive instructions.

I am deeply grateful to Professor Yukunori Korogi, chairman of the department of Radiology, university of Occupational and environmental Health School of medicine and to Professor Kazuo Awai Chairman of department of Diagnostic Radiology Graduate School of Medical Sciences, Kumamoto University, who has instructed me during the process of my study.

My great thanks are due to Dr. Toshinori Hirai, Assistant Professor of department of Diagnostic Radiology Graduate School of Medical Sciences, Kumamoto University. I have learned very much from his radiological knowledge.

Of course, I owe a great deal to the colleagues of radiology, Dr. Kitajima, Dr. Yamura, Dr. Nakayama, Dr. Katahira Dr. Hiai for their cooperation and helps in my works.

Finally special thanks are due to Dr. Yakusiji, Assistant Professor of the Department of Orthopedics department of Diagnostic Radiology Graduate School of Medical Sciences, Kumamoto University for full support.

Abbreviations

MRI: magnetic resonance imaging

DWI: Diffusion weighted imaging

ADC: apparent diffusion coefficient

FOV: field-of-view

EPI: echo planar imaging

ROI: regions of interest

CNR: contrast-to-noise ratio

T1WI: T1-weighted image

T2WI: T2-weighted image

TR: repetition time

TE: echo time

Chapter Ⅰ Background and Objectives

1. What is Diffusion in molecules?

1-1. Fick's Law

A drop of ink falling into a glass of water spreads gradually over the entire volume of water. This is a reflection of Fick's law, which states that local differences in solute concentration will give rise to a net flux of solute molecules from high concentration regions to low concentration regions.

In mathematical terms, J, the net amount of material diffusing across a unit cross-section perpendicular to a direction, here chosen as x, is proportional to the concentration gradient delta C/delta x (change in concentration per unit distance):

$$J = -D \frac{\Delta C}{\Delta x}$$

In this expression, D is the diffusion coefficient and is expressed in units of m^2/sec. The minus sign means that the material is transported in the direction of decreasing concentration.

1-2. The Random Walk

The physical process underlying the transport of material in Fick's law is the random walk motion of the molecules in a fluid: due to thermal agitation, the molecules are constantly moving and colliding with neighbors.

A molecule that is at a given location at t=0 will undergo an unpredictable succession of translations and collisions. Although we

cannot precisely locate the molecule after t=0, it remains possible to describe its average behavior over many repeats of the same experiment. On average, it will be increasingly difficult to locate the molecule. According to Einstein's law, we can expect it to end up somewhere within a sphere of radius R at time t:

$$R = \sqrt{6Dt}$$

where

D = diffusion coefficient
t = time allowed for diffusion

2. Diffusion and Magnetic Resonance Protons

2-1. In a static magnetic field

When protons are placed in a static magnetic field (B_0), they begin to precess (ie, their magnetic vector rotates about B_0). Without special preparation, the protons (spins) precessing in a static magnetic field (B_0) do not produce signal in the receiving antenna (in x-y plane) because of lack of coherence between the individual precessions (they are all out of phase and hence have no net transverse component).

2-2. 90° radio frequency (RF) pulse

By applying a 90° RF pulse, the frequency of which matches the frequency of precession of protons, the spins can be made to be in phase and have a net transverse component, producing signal in an antenna.

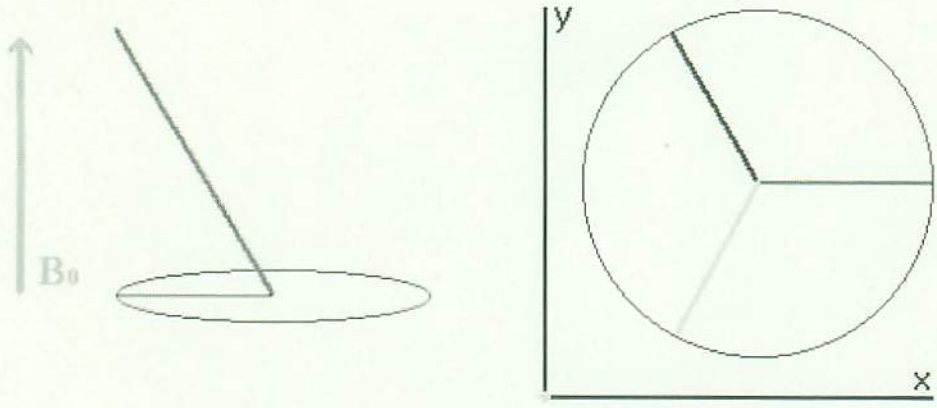

2-3. Dephasing

After the 90° RF pulse the spins will again go out of phase, mainly because of the effect of external field inhomogeneities.

2-4. Rephasing

For static spins, the dephasing caused by external field inhomogeneities can be eliminated with a 180° pulse.
This is not possible for spins undergoing diffusion because they are not static (their position fluctuates randomly because of the aleatory character of the thermal spin motion). The result is diffusion-related signal attenuation.

2-5. Pulsed Gradient Diffusion-weighted Imaging

The Stejskal-Tanner imaging sequence is used to exploit diffusion. It uses two strong gradient pulses that allow controlled diffusion weighting, according to the following equation:

$$S = S_0 e^{-bD}$$

where

S = measured signal

S_0 = signal without diffusion gradients

b = b factor

D = diffusion coefficient

For the Stejskal-Tanner sequence,

$$\text{b factor} = \gamma^2 G^2 \delta^2 (\Delta - \delta/3)$$

where

γ = 42 MHz/tesla (proton gyromagnetic ratio)

G = strength of the diffusion gradient pulses

δ = duration of the diffusion gradient pulses

Δ = time between diffusion gradient RF pulses

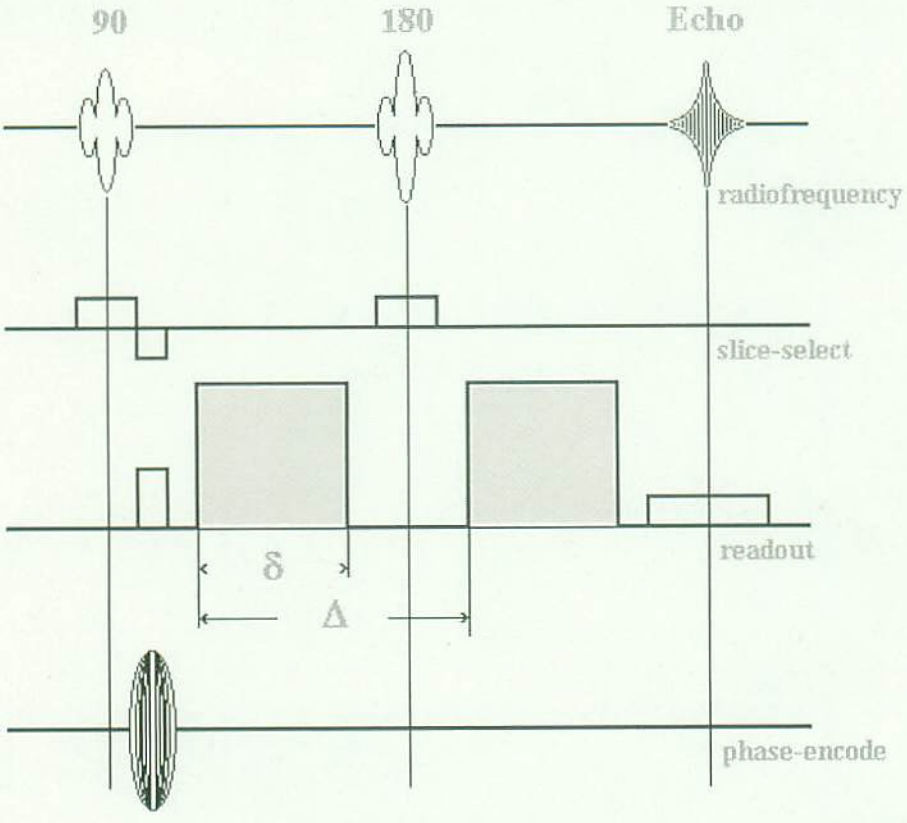

Sensitization of a spin-echo two-dimensional Fourier transform (2DFT) imaging sequence to diffusion can be easily obtained by inserting additional gradient pulses within the sequence, according to the Stejskal-Tanner scheme. These pulses (green boxes) have been put on the readout gradient axis, but they can be on any axis or combined on several axes. By changing the amplitude *G* of these gradient pulses, one can modulate the degree of diffusion weighting of the echo.

2-6. Diffusion-weighted Imaging on MRI

The effect of diffusion gradients on spin-echo images is shown in the opposite frame. Tissues with highly mobile water, such as cerebrospinal

fluid (CSF) (strong diffusion) appear dark on images acquired in the presence of strong diffusion gradients, reflecting the dephasing of the contributing spins.

Signal intensity on a diffusion-weighted image is defined by the formula

$$S = S_0 e^{-bD}$$

S_0, and hence the diffusion-weighted image, still contains contributions from spin density and relaxation times T1 and T2; therefore, the hyperintense lesion on a diffusion-weighted image may reflect a strong T2 effect (T2 "shine-through" effect) instead of reduced diffusion

2-7. Apparent diffusion map (ADC)

As previously discussed, the signal intensity on diffusion-weighted images also depends on the spin density, T1, T2, TR, and TE. To eliminate these influences and obtain pure diffusion information, we can calculate diffusion coefficient maps. A diffusion map can be calculated by combining at least two diffusion-weighted images that are differently sensitized to diffusion but remain identical with respect to the other parameters, spin density, T1, T2, TR, and TE. By using, for instance, the image S_0 without diffusion weighting (b=0) and one diffusion-weighted image (b > 0), we can calculate a D value for each pixel with the equation

$$D = -\frac{1}{b} \ln \frac{S}{S_0}$$

A parametric image containing these data is called a diffusion map or apparent diffusion map (ADC). The latter term emphasizes the fact that the *D* values obtained with this procedure depend on the experimental conditions (eg, direction of the sensitizing gradient and diffusion time delta).

3. Applications of Diffusion weighted MR imagings

Acute Infarction

Early (within the first 6 hours after stroke) CT signs of brain ischemia are subtle and difficult to detect . On conventional MR images, early (within the first 6 hours after stroke) morphologic signs (produced by tissue swelling) are detected in 50% of acute infarctions; however, signal abnormalities are not detected. With diffusion-weighted imaging of acute infarction (within the first 6 hours after stroke), 94% sensitivity and 100% specificity have been reported.

4. What is the adequate b value? Phantom study

4-1. purpose

To examine the effect of varying the diffusion encoding strength (*b* value) on the contrast (signal difference, ΔS) during diffusion-weighted magnetic resonance imaging (DWI).

4-2. Materials and Methods

We evaluated ADC values of the phantoms (DMSO, water, acetone) with diffusion values approximating in human body normal tissues at varying *b* values (0-3000 mm^{-2} second) and investigate which ADC value was adequate for evaluating human body diffusions.

ADC maps were automatically generated on the operating console using all seven images. The ADC values were calculated using the following equation:

$$ADC = -\log (SI / SI_{b=0})/b$$

where *b* reflects duration and strength of the diffusion gradient, SI is the signal intensity on the trace-weighted diffusion-weighted image (i.e., having *b* values of 0-3000 sec/mm^2), and $SI_{b=0}$ is the signal intensity on a baseline image before application of a diffusion gradient. The ADC values were obtained by measuring the intensity of the map.

Regions of interest (ROIs) were manually drawn on one ADC map in areas.

4-3.Results

All scans were performed on a 1.5-Tesla MR scanner (Achieva Nova Dual, Philips Medical systems Nederland). Theoretical ADC value of the DMSO, water and acetone was $0.62 \times 10^{-3}\ m^2/s$, $2.08 \times 10^{-3}\ m^2/s$, $4.91 \times 10^{-3}\ m^2/s$ at 23℃ and $0.65 \times 10^{-3}\ m^2/s$, $2.35 \times 10^{-3}\ m^2/s$, $5.12 \times 10^{-3}\ m^2/s$ at 37℃ respectively.

ADC value of DMSO did not decrease at high b-values. ADC value of water decreased at the b-value of 1300 mm^{-2} second in 37℃. ADC value of acetone decreased at the b-value of 800 mm^{-2} second in 37℃(Figure 1,2,3)

All phantoms showed stable ADC values at the b values from 300 to 800 mm^{-2} second in 37℃. DMSO and water showed stable ADC values from

300 to 1300 mm^{-2} second in 37°C.

4-4. Discussion

The dependence of signal intensity on diffusion when using DW MR imaging (DWI) is controlled by *b* value, which is a function of diffusion gradient strength, the duration of the gradient, and the interval between diffusion gradients, but independent of the main magnetic field strength of the system. Current gradient technology has allowed clinical hardware to achieve rapid multislice imaging and *b* values of 3000 mm^{-2} second or more. However, theoretical calculations show that at very high *b* values, the difference in signal between pathologic lesions and normal tissue may not be optimal.

In our study, all phantoms showed stable ADC values at the b value from 300 to 800 mm^{-2} second. Human body tissues normally showed lower ADC value than that of water. DMSO and water showed stable ADC value from 300 to 1300 mm^{-2} second.

This phantom study showed that we could use the b-value from 300 to 1300 mm^{-2} second to calculate accurate ADC values at the human body diffusion.

4-5. Conclusions

Our basic study showed that we could use the b-value from 300 to 1300 mm^{-2} second to calculate accurate ADC values at the human body diffusion imaging.

5. Objectives

Diffusion-weighted magnetic resonance imaging (DW-MRI), which permits the quantitative assessment of water diffusion in tissues, is used to measure the apparent diffusion coefficient (ADC) that reflects the mobility of water molecules in tissues. Diffusion-weighted imaging (DWI) has been used successfully to diagnose acute stroke and distinguish between different components of brain tumors . In musculoskeletal systems, some studies of DWI have been reported but a few.

On conventional MRI, it is sometimes difficult to histological characterization because the most tumors shows hyperintenisity on T2W images, hypointensity on T1W images and enhancement on Gd-enhanced -T1WI.

The purpose of our study was to assess the potential usefulness of DW-MRI for differentiating diagnosis in neoplasms and we performed clinical and histological studies.

Chapter Ⅱ Usefulness of DW images of metastatic brain tumors;

1 Diffusion-weighted Imaging of Metastatic Brain Tumors: Comparison with Histologic Type and Tumor Cellularity

1-1 Abstract

1-2 Introduction

1-3 Materials and methods

1-4 Results

1-5 Discussion

1-6 Conclusions

1-1 Abstract

BACKGROUND AND PURPOSE: On diffusion-weighted imaging (DWI), metastatic tumors of the brain may exhibit different signal intensity (SI) depending on their histology and cellularity. The purpose of our study was to examine the hypothesis that their SI on DWI may be related to their histology. We also sought to test the hypothesis that the tumor cellularity may correlate with the apparent diffusion coefficient (ADC) values.

MATERIALS AND METHODS: We assessed conventional MR images, DWI and ADC maps of 26 metastatic brain lesions from 26 patients, 13 of whom underwent surgery after the MR examination. Two radiologists performed qualitative assessment by consensus of the SI on DWI in areas corresponding to their enhancing portions. We measured the contrast-to-noise ratio (CNR) on T2-weighted images and normalized ADC (nADC) values, and compared them with tumor cellularity.

RESULTS: The mean SI on DWI and the CNR on T2-weighted images were significantly lower in well differentiated than poorly differentiated adenocarcinomas and lesions other than adenocarcinoma. The mean nADC value was significantly higher in well differentiated than poorly differentiated adenocarcinomas and lesions other than adenocarcinoma. All 3 small cell carcinomas and 1 large cell neuroendocrine carcinoma exhibited high SI on DWI. The nADC value showed a significant inverse correlation with tumor cellularity. There was no significant correlation between the CNR and tumor cellularity.

CONCLUSION: On DWI, well differentiated adenocarcinomas tended to be hypointense; small cell and large cell neuroendocrine carcinomas showed hyperintensity. The cellularity of the metastatic brain tumors may

be reflected in their ADC value.

1-2 Introduction

The estimated annual incidence of central nervous system (CNS) metastasis is about 8.3 per 100,000 per year, similar to the reported incidence of new primary brain neoplasms. Although metastatic tumors of the brain can be usually diagnosed with the patient's clinical information and imaging studies, some metastatic brain lesions cannot be differentiated from high-grade glioma, lymphoma, abscess, tumefactive multiple sclerosis, and subacute infarction on conventional magnetic resonance imaging (MRI)(2).

On conventional MRI, the histology of metastatic tumors of the brain may affect their signal intensity (SI) (3, 4). In addition, their components (i.e. solid tumor, degeneration, hemorrhage, and cyst) manifest various SI on MRI. On diffusion-weighted imaging (DWI), different SI of these tumors has been reported (5-10). These tumors can mimic brain abscesses or early brain infarction on DWI(6, 10). For an interpretation of the SI of brain metastasis on DWI, an understanding of its background is required.

Although the SI on DWI of the solid portion of brain metastases may be associated with their histology and tumor cellularity, these relationships remain to be investigated systematically. We hypothesized that their SI on DWI may be related to their histologic types. We also hypothesized that the tumor cellularity may correlate with the SI on T2-weighted images or the apparent diffusion coefficient (ADC) values. The purpose of our study was to determine whether these hypotheses are correct using the MRI data of our institution and neurosurgically confirmed histologic results.

1-3 Materials and Methods:

Subjects

Among 21,600 consecutive patients underwent MRI examination in our institution between January 1999 and January 2005, 2,280 patients were performed to rule out brain metastasis. Of these, 285 patients with MRI findings of suspected brain metastasis were identified in the MRI database. DWI was not routinely performed for all patients with clinically suspected brain metastasis. We performed DWI in patients of having a large T2 prolonged lesion or solitary mass in the brain. Thus, 58 of 285 patients underwent conventional MRI and DWI. We excluded 32 patients with the following conditions: MRI evidence of intratumoral hemorrhage (n = 14), previous treatment of chemotherapy, radiotherapy or biopsy for brain lesions prior to data acquisition (n = 8), histologically identified primary brain tumors (n = 3), no definite histologic diagnosis of extra-CNS malignant lesions (n = 3), no availability for review of digital data from conventional MRI and DWI (n = 2), and microscopical hemorrhage in cases with available histologic specimens of the brain lesions (n = 2). Our institutional review board approved this study and a written informed consent was obtained for MR examination.

MR Imaging

All MRI scans were obtained with a 1.5-T superconducting system (Magnetom Vision; Siemens, Erlangen, Germany). Conventional MRI and DWI were acquired during the same procedure. Conventional MRI study consisted of a sagittal T1-weighted localizing sequence (TR/TE/excitations 15/6/1), and axial T1-weighted (670/14/1), fast spin-echo T2-weighted (TR/TE_{eff}/excitation 3500/96/2; echo train length 7), and fluid-attenuated inversion-recovery (FLAIR) (TR/TE_{eff}/inversion time 6,000/120/2,000; echo train length 17) sequences, and triplanar contrast-enhanced

T1-weighted sequences. The T1-weighted, T2-weighted and FLAIR sequences were acquired at a section thickness of 5 mm with a 1-mm intersection gap, a 256 x 256-512 matrix, and a 22-cm field of view (FOV).

DWI was performed in the transverse plane by using a spin-echo echo planar imaging sequence with the following parameters: TR/TE/inversion time, 12000/100/2200; diffusion gradient encoding in 3 orthogonal directions; b=1000 sec/mm^2; FOV, 220mm; matrix size, 128 x 128 pixels; section thickness, 5 mm; section gap, 1 mm; and number of signals acquired, 1. DWI scans were performed before contrast-enhanced T1-weighted imaging.

The ADC values were calculated as follows: ADC = $-[\ln(S/S_0)]/b$, where S is the SI of the region of interest (11) obtained through 3 orthogonally oriented DWIs or diffusion trace images, S_0 is the SI of the ROI acquired through reference T2-weighted images, and b is the gradient b factor with a value of 1000 s/mm^2. ADC maps were calculated on a pixel-by-pixel basis.

Image Evaluation

Qualitative assessment of the SI on DWI in areas corresponding to the enhancing portion of the lesions on contrast-enhanced T1-weighted images was performed by the consensus of 2 experienced neuroradiologists who were blinded to the clinical and pathological information. In cases with multiple lesions, the largest lesion was selected for evaluation. The SI of the lesions was divided into 5 scales: grade -2, hypointense relative to the normal-appearing white matter; grade -1, isointense relative to the normal-appearing white matter; grade 0, isointense relative to the normal-appearing cortical gray matter; grade +1, slightly hyperintense

relative to the normal-appearing cortical gray matter; grade +2, hyperintense relative to the normal-appearing cortical gray matter.

On T2-weighted images and ADC maps of areas corresponding to the enhancing portion of the lesions on contrast-enhanced T1-weighted images, 5 uniform regions of interest (ROIs) consisting of more than 20 pixels were manually drawn by one experienced radiologist to obtain the SI on T2-weighted images and the ADC values. The ROIs were carefully placed on the solid portion to avoid volume averaging with cystic or degenerative regions that may influence the quantitative data. The mean of the 5 ROI measurements was recorded as a representative value for each case. The same method was applied to a corresponding site in the contralateral white matter judged as normal on both contrast-enhanced T1- and T2-weighted images. On T2-weighted images, image noise measurement was performed by recording the standard deviation (SD) of the SI within a ROI outside the head (i.e. in air). The contrast-to-noise ratio (CNR) for T2-weighted images was calculated as follows: CNR = (SIt - SIc)/SDnoise, where SIt is the SI of the tumor, SIc the SI of the contralateral white matter, and SDnoise the SD of the SI of air. The normalized ADC (nADC) ratio was calculated as the ratio of the mean ADC of the tumor divided by the mean ADC of the corresponding contralateral area.

Tumor cellularity (nuclear density), analyzed with NIH Image software (version 1.0.0.1) on a Windows computer, was defined as the total area of nuclei of tumor cells divided by the area of the histologic section (original magnification x200). One radiologist (S.M.) measured nuclear density of the representative area 3 times in each specimen. A mean value of the measurements for each lesion was used as the representative value

for each case.

Statistical Analysis

We performed statistical analysis of the qualitative and quantitative evaluation for all brain lesions and histologically confirmed brain lesions. For qualitative analysis, we performed Mann-Whitney's U-tests to assess the differences in the SI on DWI between well differentiated and poorly differentiated adenocarcinomas, between well differentiated adenocarcinomas and tumors with a different histology. and between poorly differentiated adenocarcinomas and tumors with a different histology.

In our quantitative analysis of the CNR and the nADC value, we performed unpaired t-tests to assess differences between the well differentiated and poorly differentiated adenocarcinomas, between well differentiated adenocarcinomas and tumors with a different histology, and between poorly differentiated adenocarcinomas and tumors with a different histology. We used the Pearson correlation tests to evaluate the correlation between tumor cellularity and the nADC value, and between tumor cellularity and the CNR on T2-weighted images. A p-value of less than 0.05 was considered to indicate a statistically significant difference.

1-4 Results:

A total of 26 patients, 15 men and 11 women ranging in age from 26 to 81 years (mean, 57.9 years), were included. Of these; 13 patients underwent surgical resection of the brain tumors after MRI study. The 13 patients were 8 men and 5 women ranging in age from 26 to 73 years (mean, 57.0 years). The summary of these lesions is shown on Tables 1 and 2. Since serous adenocarcinomas are considered to be well differentiated

adenocarcinomas, we classified 2 serous adenocarcinomas from the ovary and uterus as well differentiated adenocarcinomas. All adenocarcinomas except these 2 derived from the lung. The interval between DWI study and surgery ranged from 0 to 7 (mean ± SD, 3.3 ± 2.4) days in the 13 operated patients.

Figure 1 shows the comparison of the SI on DWI for all 26 metastatic tumors categorized according to their histology. Of the six well differentiated adenocarcinomas, 3 were grade -1, 2 were grade -2, and 1 was grade 0; 4 of 6 poorly differentiated adenocarcinomas were grade +1, the other 2 were grade 0 (Figs 2 and 3). The mean SI on DWI was significantly lower in well differentiated than poorly differentiated adenocarcinomas (p = 0.0065) and lesions other than adenocarcinoma (p = 0.0017) (Figs 2 and 3). There was no statistically significant difference for the mean SI between poorly differentiated adenocarcinomas and lesions other than adenocarcinoma (p = 0.46). All 3 small cell carcinomas and a large cell neuroendocrine carcinoma were ranked as grade +2 (Figs 4 and 5), a malignant melanoma as grade -1, and other tumors as grade 0 or +1.

Figure 6 shows the distribution of the CNR on T2-weighted images and the nADC values of the 26 metastatic tumors grouped according to their histology. The mean CNR of well differentiated adenocarcinomas (12.5 ± 11.3) was significantly lower than of poorly differentiated adenocarcinomas (39.3 ± 20.3, p = 0.015) and of tumors of the other histologic type (35.9 ± 16.4, p = 0.006). There was no statistically significant difference for the mean CNR between poorly differentiated adenocarcinomas and lesions other than adenocarcinoma (p = 0.61). The mean nADC values of well differentiated adenocarcinomas (1.81 ± 0.36) was significantly higher than that of poorly differentiated adenocarcinomas

(1.40 ± 0.27, p = 0.04) and that of tumors of other histologic types (1.19 ± 0.36, p = 0.003) (Fig 6). There was no statistically significant difference for the mean nADC between poorly differentiated adenocarcinomas and lesions other than adenocarcinoma (p = 0.36). Of 3 small cell carcinomas, 2 exhibited the lowest nADC among all 26 tumors. A large cell neuroendocrine carcinoma exhibited a low nADC and a high CNR, and a malignant melanoma had a low CNR and low nADC value.

Figure 7 shows the comparison of the SI on DWI for histologically confirmed 13 brain tumors categorized according to their histology. All 4 well differentiated adenocarcinomas were grade -2 or -1, and all 2 poorly differentiated adenocarcinomas grade +1 (Figs 2 and 3). The mean SI on DWI was significantly lower in well differentiated adenocarcinoma than lesions other than adenocarcinoma (p = 0.0082).

Figure 8 shows the distribution of the CNR on T2-weighted images and the nADC values of histologically confirmed 13 brain lesions grouped according to their histology. The mean CNR of well differentiated adenocarcinomas (15 ± 10.9) was lower than that of poorly differentiated adenocarcinomas (39 ± 9.9). The mean CNR of the well differentiated adenocarcioma was significantly lower than lesions other than adenocarcinoma (42.1 ± 9.3, p = 0.0017). The nADC of 4 well differentiated adenocarcinomas ranged from 1.48 to 2.26 (1.92 ± 0.33) and that of 2 poorly differentiated adenocarcinomas from 1.45 to 1.5 (1.48 ± 0.35). The mean nADC of the well differentiated adenocarcioma was significantly higher than lesions other than adenocarcinoma (1.28 ± 0.44, p = 0.03).

As shown in Figure 9, the nADC value was inversely correlated with tumor cellularity (r = -0.70, p = 0.0059). On the other hand, there was no

correlation between tumor cellularity and SI on the T2-weighted images (r = 0.41, p = 0.17).

1-5.Discussion:

On DWI, well differentiated adenocarcinomas tended to show hypointensity relative to gray matter. In addition, they manifested significantly lower SI than poorly differentiated adenocarcinomas and tumors of other histologic types. The SI on DWI is influenced by T2, the ADC, b value, spin density, and TE (12). All 6 well differentiated adenocarcinomas had a low CNR on T2-weighted images and high nADC values; the b value and TE were constant in our study. T2 shortening occurs in the presence of hemorrhage, however, the lesions were free of apparent hemorrhage on MRI and the surgical specimens did not yield evidence of hemorrhage. Therefore, we postulate that the hypointensity of the well differentiated adenocarcinomas was associated with an inherently low T2 and high water diffusibility in the tissues, both of which resulted in decreased SI on DWI.

The reason of the hypointensity of metastatic brain adenocarcinomas on T2-weighted images remains to be elucidated(3). Carrier et al(4), who studied the blood products, calcium, mucin, and iron in 14 patients with metastatic adenocarcinomas, concluded that their appearance on MRI most likely reflected the inherent T2 effect of the tissue. However, they did not group the tumors according to their degree of differentiation in their evaluation of the T2-weighted images. We found that well differentiated adenocarcinomas manifested a significantly lower CNR on T2-weighted images than did poorly differentiated adenocarcinomas, suggesting that the degree of differentiation may be relevant in their SI on T2-weighted images.

The well differentiated adenocarcinomas in our series derived from the lung, ovary, and uterus. Other investigators(3, 4) reported that metastatic brain lesions originating from the colon, lung or breast manifested T2 hypointensity. These results suggest that the histology of the metastatic adenocarcinomas rather than the organ harboring the primary tumor may play a role in its SI.

While others(5, 10) reported that small cell carcinomas showed hyperintensity on DWI and low ADC values, the reason for their high signal intensity remains unknown. In our series, all 3 small cell carcinomas and 1 large cell neuroendocrine carcinoma, considered to be highly aggressive poorly differentiated lung neuroendocrine tumors(13), were hyperintense on DWI. They exhibited high cellularity and low ADC values and they tended to have a higher CNR on T2-weighted images. We postulate that their hyperintensity on DWI is the result of synergistic effect of restricted diffusion and T2 shine-through.

Other lesions that had low nADC values of about 1.0 were poorly differentiated adenocarcinoma, papillotubular carcinoma, sarcoma, and malignant melanoma. Unlike the small cell carcinomas, they did not manifest hyperintensity of grade +2 on DWI; a partial explanation for this finding may be their relatively low SI on T2-weighted images. On the other hand, 1 of 2 papillotubular carcinomas with a low ADC value and a high CNR on T2-weighted images was not hyperintense of grade +2 on DWI, indicating that larger studies are required to elucidate the mechanisms that underlie the SI on DWI.

The nADC value of the tumors was significantly correlated with tumor cellularity: our small cell carcinomas and large cell neuroendocrine carcinoma exhibited high tumor cellularity. Gliomas and meningiomas

manifested a good correlation between the ADC value and tumor cellularlity (8, 14-16). We postulated that the cellularity of metastatic brain tumors may contribute to their ADC values. Our finding that there was no significant correlation between their SI on T2-weighted images and tumor cellularity suggests that various factors affect the SI on T2-weighted images, including paramagnetic (e.g. iron, calcification, hemorrhagic components, melanin), nonparamagnetic (e.g. protein concentration, fibrocollagenous stroma, flow-related signal change), and other factors (e.g. scant cytoplasm, dense cellularity). Thus, it appears unlikely that the cellularity of metastatic brain tumors can be estimated based on their SI on T2-weighted images.

There are some limitations to our study. First, one half of the metastatic tumors were without histologic confirmation for the brain tumors. The qualitative and quantitative results for all 26 lesions were similar to those for the histologically confirmed 13 brain lesions. Therefore, we believe that our results reflect a tendency of the signal intensity on DWI for brain metastases.

Second, we could not rule out the presence of tiny, undetected intratumoral hemorrhagic components that may have affected the results of our study although on conventional MRI and DWI there was no evidence of hemorrhage. In addition, 13 surgical specimens were available for histologic assessment and none exhibited evidence of hemorrhage.

Third, partial volume effects could have affected our quantitative ROI measurements. However, although intratumoral cystic and degenerative changes have the potential to affect quantitative values, it is unlikely that such areas were present within the measured ROI because the DWI and T2-weighted images a had high spatial resolution (voxel size 1.72 x 1.72

mm and 0.86 x 0.43 mm, respectively), and cysts and degenerative changes would have been recognized by the evaluators.

Finally, the original site of the examined surgical specimens may not have coincided with the site of the ROI measurement. For our quantitative analysis of tumor cellularity we chose a representative area in the solid portion of the specimens. To obtain the ROI measurements on MRI we calculated the mean value of 5 uniform ROIs in the solid portion of each tumor. Therefore, we believe that these data were derived from the representative areas in the solid portion of the metastatic brain tumors.

1-6 Conclusion:

On DWI, the enhancing areas of metastatic brain tumors of different histologic types demonstrated different SI. Well differentiated adenocarcinomas tended to be hypointense; their SI was significantly lower than that of tumors with a different histology. Our 3 small cell carcinomas and 1 large cell neuroendocrine carcinoma manifested hyperintensity on DWI. The cellularity of metastatic brain tumors may contribute to their ADC values.

Chapter Ⅲ Usefulness of DW images of primary bone tumors

1. Evaluation of diffusion-weighted imaging for the differential diagnosis of poorly contrast-enhanced and T2-prolonged bone masses: initial experience

1-1 Abstract

1-2 Introductions

1-3 Material and Methods

1-4 Results

1-5 Discussion

1-6 References

2. Monitoring response of the therapy in musculoskeletal tumors Usefulness of Diffusion weighted imaging

2-1 Abstract

2-2 Introductions

2-3 Material and Methods

2-4 Results

2-5 Discussion

2-6 References

General conclusion

1 Evaluation of diffusion-weighted imaging for the differential diagnosis of poorly contrast-enhanced and T2-prolonged bone masses: initial experience

1-1 **Abstracts**

Purpose: To determine whether quantitative diffusion-weighted magnetic resonance imaging (DW-MRI) is useful for characterizing poorly contrast-enhanced and T2-prolonged bone masses.

Materials and Methods: We studied 20 bone masses that showed high signal intensity on T2-weighted images and poor enhancement on contrast-enhanced T1-weighted images. They included 8 solitary bone cysts, 5 fibrous dysplasias, and 7 chondrosarcomas. To analyze diffusion changes we calculated the apparent diffusion coefficient (ADC) for each lesion.

Results: The ADC values of 2 types of benign lesions and (17)chondrosarcomas were not significantly different. However, the mean ADC value of solitary bone cysts (mean ±SD, $2.57 \pm 0.13\times10^{-3}$ mm^2/s) was significantly higher than that of fibrous dysplasias and chondrosarcomas ($2.0 \pm 0.21\times10^{-3}$ mm^2/s and $2.29 \pm 0.14\times10^{-3}$ mm^2/s, respectively, $p<0.05$). None of the lesions with ADC values lower than 2.0×10^{-3} mm^2/s were chondrosarcomas.

Conclusion: Although there was some overlapping in the ADC values of chondrosarcomas, solitary bone cyst, and fibrous dysplasia, quantitative DW-MRI may aid in the differential diagnosis of poorly contrast-enhanced- and T2-prolonged bone masses.

1-2 Introductions

Diffusion-weighted magnetic resonance imaging (DW-MRI), which permits the quantitative assessment of water diffusion in tissues, is

used to measure the apparent diffusion coefficient (ADC) that reflects the mobility of water molecules in tissues(18). Diffusion-weighted imaging (DWI) has been used successfully not only to diagnose acute stroke (11, 19, 20) but also to distinguish between different components of brain tumors(21, 22). It has been suggested that DWI might yield diagnostic clues, differentiating "ring-enhancing" brain masses including brain abscesses and gliomas (23-26). Tsuruda et al.(22) reported that DW-MRI was useful for distinguishing arachnoid cysts from epidermoid tumors and diffusion measurements of tumors in other organs have also been reported. In musculoskeletal systems, a study by Lang et al. (27)who studied osteogenic sarcoma in rats, indicated that DWI can accurately differentiate between viable and necrotic tumor regions. According to Baur et al.(28), diffusion measurements in human spine could reliably differentiate acute, benign- from neoplastic vertebral compression fractures. These studies suggest the potential usefulness of DW-MRI for differentiating between benign and malignant tumors in any organs.

As most bone tumors can be reliably diagnosed by radiography and clinical data, additional imaging studies are usually not necessary. MRI is generally accepted as a valuable method for evaluating bone tumor extension. Although MRI studies are usually unnecessary for characterizing bone tumors, because they provide superior soft tissue contrast, they may reveal the pathology of the underlying processes(28). MRI has proven especially advantageous for identifying non-mineralized chondroid matrix, vascular tissue, cysts, and hemosiderotic tissue(29). However, on conventional MRI, it is usually difficult to characterize cystic lesions, lesions with cartilaginous, myxomatous, or hyaline changes, and

atypical connective tissue tumors because all of these lesions appear as markedly hyperintense areas on T2-weighted images and as poorly enhanced areas on contrast-enhanced T1-weighted images. It is important to differentiate these bone masses from malignant bone tumors, especially chondrosarcomas. As the appearance of solitary bone cysts and fibrous dysplasia on MRI and radiographs can be similar to that of chondrosarcomas , DWI, which discloses water diffusion in bone lesions, may be useful for their differentiation. We undertook this study because to our knowledge, there currently are no reports that evaluate the usefulness of DWI for differentiating such bone lesions.

1-3 Materials and Methods

Patients

Written prior informed consent was obtained from all patients or their parents for performance of radiologic studies and analysis of clinical data. Our institutional review board approved this study protocol.
We performed a retrospective study of 20 bone lesions from 20 consecutive patients examined between February 2000 and April 2003. There were 8 solitary bone cysts, 5 fibrous dysplasias, and 7 chondrosarcomas. The lesions manifested markedly T2-prolonged and poorly-enhanced areas on MRI. None exhibited the typical appearance on clinical or radiographic findings: solitary bone cysts were seen in elderly patients; fibrous dysplasias had osteolytic area without ground-grass appearance; chondrosarcomas did not have calcification or lobulated appearance. The diagnosis of all masses was confirmed by histologic biopsy and/or surgery after MRI study. All patients underwent DW-MRI and spin-echo MRI. The patients, 12 males and 8 females, ranged in age from 6 to 72 years

(mean 34.9 years). Their lesions measured between 3.0 and 17.0 cm in diameter (median 7.1 cm), 5 were located in the upper arm, 9 in the upper leg, and 2 each in the pelvis, lower leg, and ribs.

MRI studies

All studies were performed using a circular polarized (CP) Extremity, CP Flex large phased-Array, or CP Body-Array coil and a 1.5T MR imager (Symphony, Siemens Erlangen, Germany). In all patients, T1-, T2-, and DW images and contrast-enhanced T1-weighted images were obtained in the coronal, axial and/or sagittal plane. T1-weighted images (spin echo, TR/TE/number of excitation = 500msec/12msec/1) and T2-weighted images (fast spin echo, TR/TE/Turbo factor/flip angle/ band width / number of excitation = 3500-4000msec/120msec/15/180º/120 kHz /2] were obtained; the slice thickness was 4-5 mm, the inter-slice gap 0.2 mm, field-of-view (FOV) 180-250 mm, and matrix 512×256 pixels. Then, gadopentetate dimeglumine (0.1 mmol/kg body weight) was administered and T1-weighted sequences were obtained.

DWI was performed in the axial or sagittal plane using a spin-echo echo planar imaging (EPI) sequence with the following parameters: TR/TE = 4504msec/105msec, 25 m/Tm gradient strength, 220 mm FOV, 128 x 64 pixel matrix size, 5 mm section thickness, 0.2 mm section gap, and number of signals acquired, one. DW images were acquired with motion-probing gradient (MPG) pulses applied sequentially along three (x, y, and z axes) directions with three b factors (0, 500, and 1000 seconds/mm^2). Three DWI were obtained within an acquisition time of 36 sec. In all images a fat-saturated pulse was used to exclude severe chemical-shift artifacts.

ADC maps were automatically generated on the operating console

using all seven images. The ADC values were calculated using the following equation:

$$ADC = -\log (SI / SI_{b=0})/b$$

where *b* reflects duration and strength of the diffusion gradient, SI is the signal intensity on the trace-weighted diffusion-weighted image (i.e., having *b* values of 500, 1000 sec/mm^2), and $SI_{b=0}$ is the signal intensity on a baseline image before application of a diffusion gradient. The ADC values were obtained by measuring the intensity of the map.

Three uniform regions of interest (ROIs) were manually drawn on one ADC map in areas corresponding to the non-enhancing and T2-prolonged portion of lesions. This was done to avoid volume-averaging with enhanced or T2-shortened regions that would influence the ADC values. One radiologist (Y.H.) without knowledge of the histopathologic findings chose the ADC map that showed the most representative lesions. Three ADC values, measured by that radiologist were averaged to determine the ADC value for each lesion. The same radiologist obtained another measurement in the same fashion 6 months after the first.

Statistical Analysis

Intraobserver variation of ROI measurement was analyzed using paired Student's *t*-test.

Mean ADC values were compared between benign and malignant bone lesions using Student's *t*-test. *P* values less than 0.05 were considered to indicate a statistically significant difference. We also statistically compared the ADC values of simple bone cysts, fibrous dysplasia, and chondrosarcomas by one-way analysis of variance. When

the overall differences were statistically significant, post hoc analysis was performed using Sheffes' method. *P* values less than 0.05 were considered to reflect a statistically significant difference.

1-4 Results

Assessment of intraobserver variation of ROI measureaments revealed no significantly difference.

The mean ADC values of chondrosarcomas and benign bone masses were $2.29 \pm 0.14\times10^{-3}mm^2/s$ and $2.37 \pm 0.31\times10^{-3}mm^2/s$ (mean ±SD), respectively (Figs. 1-3). There were no significant differences in the mean ADC values between chondrosarcomas and benign bone masses (Fig. 4). In ANOVA, there was a significant difference in the mean ADC values among fibrous dysplasias, simple bone cysts, and chondrosarcomas ($p=0.0002$). In multiple comparisons, the mean ADC value of simple bone cysts ($2.57 \pm 0.13\times10^{-3}$ mm^2/s) was significantly higher than that of fibrous dysplasias or chondrosarcomas ($2.0 \pm 0.21\times10^{-3}$ mm^2/s and $2.29 \pm 0.14\times10^{-3}$ mm^2/s, respectively, $p<0.05$). While the mean ADC value of chondrosarcomas tended to be higher than that of fibrous dysplasias, the difference was not statistically significant ($p=0.054$) (Fig. 5). Although there was some overlap in the ADC values among fibrous dysplasias, simple bone cysts, and chondrosarcomas, no lesions with ADC values lower than 2.0×10^{-3} mm^2/s were chondrosaracomas.

1-5 Discussion

Although examinations of the usefulness of DWI to study the abdomen and musculoskeletal system have primarily employed animal models, there is some evidence that DWI may be of value in humans (30).

Normal tissues such as muscle, fat, and bone marrow reportedly exhibit different diffusion characteristics (30-32) and pathologic entities such as neoplasms, post-therapeutic soft tissue changes, and inflammatory processes can be differentiated by their diffusion characteristics(30). Due to the higher mobility of water protons within muscle, normal muscle shows significantly higher diffusion values than subcutaneous fat or bone marrow (32). Van Rijswijk et al.(29) reported that the true diffusion coefficients of malignant soft-tissue tumors were significantly lower than those of benign tumors. In animal models of osteosarcoma, DWI accurately differentiated between viable and necrotic musculoskeletal lesions (27, 33).

It is important to differentiate low-grade chondrosarcomas from benign lesions in patients whose bone tumors exhibit marked hyperintensity on T2-weighted images and poor enhancement on contrast-enhanced T1-weighted images. The diagnosis of some malignant bone tumors, especially low-grade central chondrosarcomas, is difficult because radiographs fail to show the obvious features of aggressive behavior such as cortical violation and a soft tissue mass. If low-grade chondrosarcomas are located in the meta-diaphysis and not calcified in the long bones, on plain radiographs the lesions may simulate localized fibrous dysplasias, solitary bone cysts, bone infarcts or chondromas.

We used quantitative DWI and found that the difference in the mean ADC values of benign tumors and chondrosarcomas was not significantly different. On the other hand, the mean ADC value of simple bone cysts was significantly higher than that of fibrous dysplasias and chondrosarcomas. The higher water content of simple bone cysts than fibrous dysplasias and chondrosarcomas may explain their higher ADC

value. The mean ADC value of chondrosarcomas tended to be higher than that of fibrous dysplasias. As cartilaginous and tumor cells are sparse in the myxoid matrix of chondrosarcomas, water diffusion may not be inhibited in these tumors. Although necrotic tissues have high ADC value (27, 33), a significant necrosis area could not be seen in the specimen of the chondrosarcomas in our study. Fibrous dysplasias may yield various T2 signals and varying degrees of contrast enhancement depending on the amount and degree of bony trabeculae, cellularity, fibrous tissue, and cystic and hemorrhagic changes(34, 35). In our samples, fibrous dysplasias with cyst-like areas contained coarse fibrous tissues and we posit that their lower ADC values may be attributable to the inhibition of water diffusion by these tissues.

None of the lesions with ADC values lower than 2.0×10^{-3} mm^2/s were chondrosarcomas. Our observation suggests that DWI may be useful for differentiating between benign lesions and chondrosarcomas and studies with larger sample numbers are underway in our laboratory to test this hypothesis.

This study has some limitations. First, as it contained only 2 types of benign lesions, confirmation of the usefulness of DWI for differentiating between benign lesions and chondrosarcomas may require the inclusion of many types of benign lesions; i.e. chondromas. However, we did not include chondromas because most of these lesions can be easily diagnosed on plain radiographs, and because we have encounterd very few chondromas, with uncommon features. Second, the EPI sequence may produce geometric distortion and susceptibility artifacts. We used a spin-echo EPI sequence for DWI because with respect to image distortion, this technique is superior to gradient-echo EPI sequences. As we did not

encounter image distortion that affected the measurement of the ADC value of the lesions, we suggest that the spin-echo EPI sequence is suitable for the in vivo evaluation of the musculoskeletal system. Improvements in gradient field strengths, multishot techniques and the introduction of parallel imaging techniques would be helpful in maximizing spatial resolution and decreasing susceptibility artifacts(17, 36, 37). We are now using the multishot techniques to evaluate various bone lesions.

In conclusion, while we found that quantitative measurements of simple bone cysts, fibrous dysplasias, and chondrosarcoma showed some overlaps, DWI may be of use in differentiating between poorly contrast-enhanced- and T2-prolonged bone masses in vivo.

2. Monitoring response of the therapy in musculoskeletal tumors

Usefulness of Diffusion weighted imaging

2-1 Abstract

OBJECTIVE. The purpose of our study was to investigate whether quantitative diffusion weighted images (DWIs) is useful for monitoring the therapeutic response of primary bone tumors on unenhanced MRI.

MATERIALS AND METHODS. We encountered 14 patients with 14 histologically confirmed osteogenic and Ewing sarcomas. Diffusion weighted- and spin-echo MR images were performed in all patients before and after therapy. We measured the apparent diffusion coefficient (ADC) values, contrast-to-signal-noise ratio (CNR) on T2-weighted image and tumor volume of the bone tumors pre- and post-treatment and we determined, Change in ADC value (%), Change in CNR (%), and Change in tumor volume (%), respectively. The 14 bone tumors were divided into 2 groups based on their treatment response (group A and group B). Change in ADC value, Change in tumor volume and Change in CNR were compared between groups A and B, using a two-tailed Student's *t*-test.

RESULTS. In our study, the change in the ADC value was statistically greater in the group that manifested tumor necrosis exceeding 90% or no tumor regrowth (group B) than in the group with less than 90% necrosis (group A) (p=0.001). On the other hand, there was no significant difference between the 2 groups with respect to changes in the CNR (p=0.849) and tumor volume (p=0.078).

CONCLUSION. The ADC value on DWI scans holds promise as a valuable tool for monitoring the therapeutic response of primary bone sarcomas.

2-2 Introductions

Induction and adjuvant chemotherapy has improved long-term survival of patients with musculoskeletal tumors such as osteogenic sarcomas from 20% to 70% compared with surgery alone (38). In osteogenic and Ewing sarcoma, the degree of necrosis following a course of induction chemotherapy and surgery is a prognostic factor for event-free survival(39), rendering the quantitative non-invasive estimation of tumor necrosis during various stages of treatment is indispensable. However, assessing the therapeutic response of malignant musculoskeletal tumors by radiological examination alone is difficult.

Diffusion-weighted magnetic resonance imaging (DW-MRI) is useful for differentiation between benign and malignant tumors in various fields including musculoskeletal system(30). Lang et al.(27) who studied a rat osteogenic sarcoma model found DW-MRI was also useful to identify necrotic regions in the tumor. Based on their findings, we hypothesized that the apparent diffusion coefficient (ADC) value measured in DWI might be a valuable indicator of the treatment response. The purpose of our study was to investigate whether quantitative DWI is useful for monitoring the therapeutic response of primary bone tumors on unenhanced MRI.

2-3 Materials and Methods

Patient Population

Between January 2001 and December 2004, we encountered 14 patients (6 males and 8 females) with 14 histologically confirmed malignant bone tumors. Their mean age was 14.4 years (range 9-20 years). Of the 14 lesions, 9 were located in the femur; 2 were located in humerus, one each was in the ilium, tibia, and fibula. There were 11 osteosarcomas and 3 Ewing sarcomas. The lesion diameter ranged from 1.9 - 13.5 cm (median 3.5 cm). All 14 tumors received chemotherapy (n=12) or radiotherapy (n=2) with (n=12) or without (n=2) surgery (Table 1).

DW- and spin-echo MRI of the femoral humeral and pelvic site was performed in all patients before and after therapy. Comparison follow-up imaging studies were obtained 10 - 35 days (mean 12.2 days) after finishing chemotherapy or radiotherapy. Twelve patients underwent definitive surgery within 3 days of the post-chemotherapy imaging study. We correlated the conventional MRI findings and ADC values on pre- and post-treatment studies with histological findings.

The response to chemotherapy of the 12 operated tumors was judged histopathologically by 2 pathologists with 16 and 22 years of experience based on the percent tumor necrosis; the response to radiotherapy of the 2 unoperated tumors was judged by their clinical course (Table 1). The 14 malignant bone tumors were divided into 2 groups based on their treatment response(40); group A (n=7) was comprised of tumors with less than 90% tumor necrosis, group B of tumors with 90% or more necrosis (n=5) and tumors without macroscopic evidence of regrowth for 2.5 years after the first

radiotherapy (n=2). Of 12 operated tumors, 5 exhibited necrosis in more than 90% of the tumor (group B); this was considered a good response. The other 7 operated tumors contained necrotic areas that comprised less than 90% of the tumor (group A) (Fig.1, Tables 1 and 2). Neither of the 2 unoperated tumors exhibited macroscopic regrowth 2.5 years after the first chemotherapy; they were classified as group B tumors.

MR Imaging

All studies were performed using a circular polarized (CP) Extremity, CP Flex large phased-Array, or CP Body-Array coil and a 1.5T MR imager (Symphony, Siemens Erlangen, Germany). In all patients, T1-, T2-, and DW images and contrast-enhanced T1-weighted images were obtained in the coronal, axial and/or sagittal plane. T1-weighted images (spin echo, TR/TE/number of excitation = 500msec/12msec/1) and T2-weighted images (fast spin echo, TR/TE/Turbo factor/flip angle/ band width / number of excitation = 3500-4000msec/120msec/15/180º/120 kHz /2] were obtained; the slice thickness was 4-5 mm, the inter-slice gap 0.2 mm, field-of-view (FOV) 180-250 mm, and matrix 512×256 pixels. Then, gadopentetate dimeglumine (0.1 mmol/kg body weight) was administered and T1-weighted sequences were obtained.

DWI was performed in the axial or sagittal plane using a spin-echo echo planar imaging (EPI) sequence with the following parameters: TR/TE = 4504msec/105msec, 25 m/Tm gradient strength, 220 mm FOV, 128 x 64 pixel matrix size, 5 mm section thickness, 0.2 mm

section gap, and number of signals acquired, one. DW images were acquired with motion-probing gradient (MPG) pulses applied sequentially along three (x, y, and z axes) directions with three b factors (0, 500, and 1000 seconds/mm^2). Three DWI were obtained within an acquisition time of 36 sec. In all images a fat-saturated pulse was used to exclude severe chemical-shift artifacts.

ADC maps were automatically generated on the operating console using all seven images. The ADC values were calculated using the following equation:

$$ADC = -\log (SI / SI_{b=0})/b$$

where *b* reflects duration and strength of the diffusion gradient, SI is the signal intensity on the trace-weighted diffusion-weighted image (i.e., having *b* values of 500, 1000 sec/mm^2), and $SI_{b=0}$ is the signal intensity on a baseline image before application of a diffusion gradient. The ADC values were obtained by measuring the intensity of the map.

Image Analysis

Evaluation of ADC value before and after treatment

The bone marrow is rich in fat and the bone cortex is rich in minerals. Because we used the fat suppression technique in DWI, the ADC of normal bone marrow was 0×10^{-3} mm^2/sec. Because mineral-rich areas have no spinning proton molecules, they usually showed null signal on MRI and their ADC tended to be 0×10^{-3} mm^2/sec (Fig. 1-a).

To avoid voxels with an ADC of 0 because of the marrow fat or thick calcified areas such as the cortex or tumor ossification, we used histograms. We transferred 2-5 ADC map images to a workstation (Advantage Windows 3.01, GE Medical Systems, Milwaukee, WI, USA) and performed histogram analysis to determine the mean ADC value of voxels containing pure tumor tissue of pre- and post-treatment malignant bone tumors, cutting off voxels with a value of 0 (Fig. 1-b).

We determined the rate of change in the ADC value using the formula

Change in ADC value (%) = ADC $value_{post}$/ADC $value_{pre}$ x 100,

where ADC $value_{pre}$ and ADC $value_{post}$ are the mean ADC values of the musculoskeletal lesions pre- and post-treatment, respectively.

Evaluation of contrast-to-signal-noise ratio (CNR) and tumor volume pre- and post-treatment

We also measured the signal intensity of the tumors on T2-weighted images to evaluate changes in the CNR between pre- and post-treatment studies by placing regions of interest at more than 3 areas within each tumor. We also determined the total lesion volume and the CNR on T2-weighted images and compared pre- and post-treatment findings.

On each slice of contrast-enhanced T1-weighted images, one

radiologist (Y.H.) with 12 years of experience with MRI manually traced the lesion, multiplied the areas by the slice thickness and gaps, and summed the areas on each slice to obtain the total lesion volume. To determine changes in the tumor volume we used the formula

Change in tumor volume (%) = tumor $volume_{post}$/tumor $volume_{pre}$ ×100

The same radiologist (Y.H.) also measured the signal intensity of tumor and muscle on T2-weighted image by placing the ROI in one slice of each patient, taking care to avoid vessel, fat, calcification, ossification and artifacts. The standard deviation (SD) of the background noise was measured in the same slices with the largest possible ROI in the phase-encoding direction outside the body to account for artifacts. CNR was calculated as

$CNR = (SI_{lesion} - SI_{muscle})/SD$,

where SI_{lesion} and SI_{muscle} are the signal intensity of the tumor and muscle, respectively, and SD is the standard deviation of the background noise.

Then we determined the change in CNR using the formula

Change in CNR (%) = CNR_{post}/CNR_{pre} x 100.

where CNR_{pre} and CNR_{post} are the CNR on T2-weighted images before and after therapy, respectively.

Statistical Analysis

The mean ADC values, CNR, and tumor volume were compared between groups A and B, using a two-tailed Student's *t*-test. *P* values less than 0.05 were considered to indicate statistically significant differences. Statistical analysis was with a statistical software package (StatView 5.0, SAS Institute Inc, Carry, NC).

2-4 Results

Change in the ADC value was statistically greater in group B than group A (p=0.001) (Fig. 2, Table 2).

There was no significant difference with respect to changes in the CNR on T2-weighted images between groups A and B (p=0.849) (Fig. 3 and Table 3).

There was no significant difference in tumor volume changes between groups A and B (p=0.078) (Fig. 4 and Table 4). The size of tumors that were mostly confined to the bone marrow tended to increase after therapy.

2-5 Discussions

In our study, the change in the ADC value was statistically greater in the group that manifested tumor necrosis exceeding 90% or no tumor regrowth (group B) than in the group with less than 90% necrosis (group A) (p=0.001). On the other hand, there was no significant difference between the 2 groups with respect to changes in the CNR (p=0.849) and tumor volume (p=0.078). These results suggest that

DWI is a promising tool for monitoring the response to therapy of primary bone sarcomas.

Viable and necrotic tumor tissues can be differentiated with the aid of DWI-MRI because in the former, the cell- and intracellular membranes are intact, thereby restricting molecular diffusion into viable tumors. In contrast, necrotic tumors are characterized by a breakdown of these membranes, thereby allowing free diffusion and an increase in the mean free path-length of the diffusing molecules. On conventional MRI, assessment of the therapeutic response of bone tumors limited to the bone marrow may be difficult because these lesions show non-specific signal-intensity changes and are often increased in size. According to Lang et al.(27) there was no significant difference on T2-weighted images between viable and necrotic tumor tissues in rat osteogenic sarcoma because the T2 relaxation times were similar. The tumor size is also not a reliable indicator of the therapeutic response because the apparent post-treatment increase may be attributable to the visualization of surrounding connective tissue, ossification, and edematous changes.

The correct assessment of the therapeutic response of malignant musculoskeletal tumors by radiological methods can be difficult. Changes in tumor volume or structure observed on conventional radiographs(41, 42) and CT scans(43) failed to predict the histological tumor response. While angiographic assessment may be more accurate (43, 44), due to its invasive nature it can be used in patients only undergoing intra-arterial chemotherapy. Unenhanced- or enhanced static MRI study is useful for precise preoperative

staging, but it fails to predict accurately the histological response. Morphological changes induced by chemotherapy may be associated with hemorrhage, necrosis, edema, and inflammatory fibrosis without specific MRI patterns(42, 45) Serial dynamic MRI studies on various primary bone tumors after neoadjuvant chemotherapy have been reported(45-51), however, overlapping complicates the confident distinction between histological responders and non responders(52). According to Dyke et al. (53)perfusion MRI was useful for determining the response to induction chemotherapy because it can predict the vascular permeability of the tumor and the vascular volume. But, dynamic MRI and perfusion MRI requires the bolus injection of Gd; this increases the total cost and examination time.

In patients with bone sarcomas treated by preoperative chemotherapy, scintigraphy has been used to detect necrosis-induced changes in the tumor uptake of thallium-201(54-56). Its accumulation indicates the viability and metabolic activity of the tumor cells. As thallium-201 scintigraphy, perfusion MRI, and DWI may have different mechanisms for monitoring the therapeutic response, studies are underway in our laboratory to determine which of these modalities is most useful.

To obtain DW-MRI scans, several techniques are employed, including gradient echo- and spin-echo sequences. We chose a spin-echo EPI sequence that, because it can be performed within a few seconds, results in fewer motion artifacts. EPI sequences usually have a lower signal-to-noise ratio and are susceptible to

artifacts; this results in image distortion and signal loss (31). Improvements in gradient field strengths and multi-shot techniques, and the introduction of parallel imaging techniques will help to maximize spatial resolution and to decrease the susceptibility to artifacts.

There are potential limitations in our study. First, the number of tumors available for study was relatively small. Second, as 2 of the 14 tumors were treated by radiation therapy alone, no histological evidence could be obtained and their post-treatment ADC values may reflect not only necrosis but also edema.

In conclusion, the ADC value on DWI scans holds promise as a valuable tool for monitoring the therapeutic response of primary bone sarcomas. Studies are underway in our laboratory to confirm the role of DWI in the post-treatment assessment of primary bone sarcomas with special focus on pathologic correlation, as the ADC value may reflect the therapeutic responses in a lager patient population.

Gerenal conclusions

Our basic study showed that we could use the b-value from 300 to 1300 mm^{-2} second to calculate accurate ADC values at the human body diffusion imaging.

In the clinical observation, we found that quantitative measurements of simple bone cysts, fibrous dysplasias, and chondrosarcoma showed some overlaps, DWI may be of use in differentiating between poorly contrast-enhanced- and T2-prolonged bone masses in vivo. Also, we found that the ADC value on DWI scans holds promise as a valuable tool for monitoring the therapeutic response of primary bone sarcomas.

Studies are underway in our laboratory to confirm the role of DWI in the post-treatment assessment of primary bone sarcomas with special focus on pathologic correlation, as the ADC value may reflect the therapeutic responses in a lager patient population.

There were some limitations of these studies. The EPI sequence may produce geometric distortion and susceptibility artifacts. We used a spin-echo EPI sequence for DWI because with respect to image distortion, this technique is superior to gradient-echo EPI sequences. As we did not encounter image distortion that affected the measurement of the ADC value of the lesions, we suggest that the spin-echo EPI sequence is suitable for the in vivo evaluation of the musculoskeletal system. Improvements in gradient field strengths, multishot techniques and the introduction of parallel imaging techniques would be helpful in maximizing spatial resolution and

decreasing susceptibility artifacts.

Resent advances in MR technology such as high-performance gradient coils, parallel imaging techniques and phased-array receiver coils have finally made diffusion-weighted imaging of the body feasible for clinical use. Applying parallel imaging, the accumulating phase that causes susceptibility artifacts is decreased because of a reduction in the train of gradient echoes and sampling time, and contributes to the suppression of motion artifacts shortening imaging times. Further investigations need to perform using parallel imaging of body diffusions.

Reference

1. Pickens DR, 3rd, Jolgren DL, Lorenz CH, Creasy JL, Price RR. Magnetic resonance perfusion/diffusion imaging of the excised dog kidney. Invest Radiol 1992; 27:287-292.
2. Ricci PE. Imaging of adult brain tumors. Neuroimaging Clin N Am 1999; 9:651-669.
3. Egelhoff JC, Ross JS, Modic MT, Masaryk TJ, Estes M. MR imaging of metastatic GI adenocarcinoma in brain. AJNR Am J Neuroradiol 1992; 13:1221-1224.
4. Carrier DA, Mawad ME, Kirkpatrick JB, Schmid MF. Metastatic adenocarcinoma to the brain: MR with pathologic correlation. AJNR Am J Neuroradiol 1994; 15:155-159.
5. Okamoto K, Ito J, Ishikawa K, Sakai K, Tokiguchi S. Diffusion-weighted echo-planar MR imaging in differential diagnosis of brain tumors and tumor-like conditions. Eur Radiol 2000; 10:1342-1350.
6. Holtas S, Geijer B, Stromblad LG, Maly-Sundgren P, Burtscher IM. A ring-enhancing metastasis with central high signal on diffusion-weighted imaging and low apparent diffusion coefficients. Neuroradiology 2000; 42:824-827.
7. Stadnik TW, Chaskis C, Michotte A, et al. Diffusion-weighted MR imaging of intracerebral masses: comparison with conventional MR imaging and histologic findings. AJNR Am J Neuroradiol 2001; 22:969-976.

8. Kono K, Inoue Y, Nakayama K, et al. The role of diffusion-weighted imaging in patients with brain tumors. AJNR Am J Neuroradiol 2001; 22:1081-1088.
9. Hartmann M, Jansen O, Heiland S, Sommer C, Munkel K, Sartor K. Restricted diffusion within ring enhancement is not pathognomonic for brain abscess. AJNR Am J Neuroradiol 2001; 22:1738-1742.
10. Geijer B, Holtas S. Diffusion-weighted imaging of brain metastases: their potential to be misinterpreted as focal ischaemic lesions. Neuroradiology 2002; 44:568-573. Epub 2002 May 2029.
11. Karonen JO, Liu Y, Vanninen RL, et al. Combined perfusion- and diffusion-weighted MR imaging in acute ischemic stroke during the 1st week: a longitudinal study. Radiology 2000; 217:886-894.
12. Hiwatashi A, Kinoshita T, Moritani T, et al. Hypointensity on diffusion-weighted MRI of the brain related to T2 shortening and susceptibility effects. AJR Am J Roentgenol 2003; 181:1705-1709.
13. Franklin WA. Pathology of lung cancer. J Thorac Imaging 2000; 15:3-12.
14. Sugahara T, Korogi Y, Kochi M, et al. Usefulness of diffusion-weighted MRI with echo-planar technique in the evaluation of cellularity in gliomas. J Magn Reson Imaging 1999; 9:53-60.
15. Guo AC, Cummings TJ, Dash RC, Provenzale JM. Lymphomas and high-grade astrocytomas: comparison of water diffusibility and histologic characteristics. Radiology 2002; 224:177-183.
16. Gauvain KM, McKinstry RC, Mukherjee P, et al. Evaluating pediatric brain tumor cellularity with diffusion-tensor imaging. AJR Am J Roentgenol 2001; 177:449-454.
17. Bammer R, Auer M, Keeling SL, et al. Diffusion tensor imaging

using single-shot SENSE-EPI. Magn Reson Med 2002; 48:128-136.

18. Le Bihan D, Breton E, Lallemand D, Grenier P, Cabanis E, Laval-Jeantet M. MR imaging of intravoxel incoherent motions: application to diffusion and perfusion in neurologic disorders. Radiology 1986; 161:401-407.
19. Gonzalez RG, Schaefer PW, Buonanno FS, et al. Diffusion-weighted MR imaging: diagnostic accuracy in patients imaged within 6 hours of stroke symptom onset. Radiology 1999; 210:155-162.
20. Marks MP, de Crespigny A, Lentz D, Enzmann DR, Albers GW, Moseley ME. Acute and chronic stroke: navigated spin-echo diffusion-weighted MR imaging. Radiology 1996; 199:403-408.
21. Tien RD, Felsberg GJ, Friedman H, Brown M, MacFall J. MR imaging of high-grade cerebral gliomas: value of diffusion-weighted echoplanar pulse sequences. AJR Am J Roentgenol 1994; 162:671-677.
22. Tsuruda JS, Chew WM, Moseley ME, Norman D. Diffusion-weighted MR imaging of the brain: value of differentiating between extraaxial cysts and epidermoid tumors. AJNR Am J Neuroradiol 1990; 11:925-931; discussion 932-924.
23. Kim YJ, Chang KH, Song IC, et al. Brain abscess and necrotic or cystic brain tumor: discrimination with signal intensity on diffusion-weighted MR imaging. AJR Am J Roentgenol 1998; 171:1487-1490.
24. Noguchi K, Watanabe N, Nagayoshi T, et al. Role of diffusion-weighted echo-planar MRI in distinguishing between brain brain abscess and tumour: a preliminary report. Neuroradiology 1999; 41:171-174.

25. Desprechins B, Stadnik T, Koerts G, Shabana W, Breucq C, Osteaux M. Use of diffusion-weighted MR imaging in differential diagnosis between intracerebral necrotic tumors and cerebral abscesses. AJNR Am J Neuroradiol 1999; 20:1252-1257.

26. Nadal Desbarats L, Herlidou S, de Marco G, et al. Differential MRI diagnosis between brain abscesses and necrotic or cystic brain tumors using the apparent diffusion coefficient and normalized diffusion-weighted images. Magn Reson Imaging 2003; 21:645-650.

27. Lang P, Wendland MF, Saeed M, et al. Osteogenic sarcoma: noninvasive in vivo assessment of tumor necrosis with diffusion-weighted MR imaging. Radiology 1998; 206:227-235.

28. Baur A, Stabler A, Bruning R, et al. Diffusion-weighted MR imaging of bone marrow: differentiation of benign versus pathologic compression fractures. Radiology 1998; 207:349-356.

29. van Rijswijk CS, Kunz P, Hogendoorn PC, Taminiau AH, Doornbos J, Bloem JL. Diffusion-weighted MRI in the characterization of soft-tissue tumors. J Magn Reson Imaging 2002; 15:302-307.

30. Baur A, Reiser MF. Diffusion-weighted imaging of the musculoskeletal system in humans. Skeletal Radiol 2000; 29:555-562.

31. Baur A, Huber A, Arbogast S, et al. Diffusion-weighted imaging of tumor recurrencies and posttherapeutical soft-tissue changes in humans. Eur Radiol 2001; 11:828-833.

32. Cleveland GG, Chang DC, Hazlewood CF, Rorschach HE. Nuclear magnetic resonance measurement of skeletal muscle: anisotrophy of the diffusion coefficient of the intracellular water. Biophys J 1976; 16:1043-1053.

33. Karczmar GS, River JN, Goldman Z, et al. Magnetic resonance imaging of rodent tumors using radiofrequency gradient echoes. Magn Reson Imaging 1994; 12:881-893.
34. Jee WH, Choi KH, Choe BY, Park JM, Shinn KS. Fibrous dysplasia: MR imaging characteristics with radiopathologic correlation. AJR Am J Roentgenol 1996; 167:1523-1527.
35. Fitzpatrick KA, Taljanovic MS, Speer DP, et al. Imaging findings of fibrous dysplasia with histopathologic and intraoperative correlation. AJR Am J Roentgenol 2004; 182:1389-1398.
36. Bammer R, Keeling SL, Augustin M, et al. Improved diffusion-weighted single-shot echo-planar imaging (EPI) in stroke using sensitivity encoding (SENSE). Magn Reson Med 2001; 46:548-554.
37. Cercignani M, Horsfield MA, Agosta F, Filippi M. Sensitivity-encoded diffusion tensor MR imaging of the cervical cord. AJNR Am J Neuroradiol 2003; 24:1254-1256.
38. de Baere T, Vanel D, Shapeero LG, Charpentier A, Terrier P, di Paola M. Osteosarcoma after chemotherapy: evaluation with contrast material-enhanced subtraction MR imaging. Radiology 1992; 185:587-592.
39. Meyers PA, Gorlick R, Heller G, et al. Intensification of preoperative chemotherapy for osteogenic sarcoma: results of the Memorial Sloan-Kettering (T12) protocol. J Clin Oncol 1998; 16:2452-2458.
40. Huvos AG, Rosen G, Marcove RC. Primary osteogenic sarcoma: pathologic aspects in 20 patients after treatment with chemotherapy en bloc resection, and prosthetic bone replacement. Arch Pathol Lab Med 1977; 101:14-18.

41. Smith J, Heelan RT, Huvos AG, et al. Radiographic changes in primary osteogenic sarcoma following intensive chemotherapy. Radiological-pathological correlation in 63 patients. Radiology 1982; 143:355-360.

42. Holscher HC, Bloem JL, Vanel D, et al. Osteosarcoma: chemotherapy-induced changes at MR imaging. Radiology 1992; 182:839-844.

43. Mail JT, Cohen MD, Mirkin LD, Provisor AJ. Response of osteosarcoma to preoperative intravenous high-dose methotrexate chemotherapy: CT evaluation. AJR Am J Roentgenol 1985; 144:89-93.

44. Kumpan W, Lechner G, Wittich GR, et al. The angiographic response of osteosarcoma following pre-operative chemotherapy. Skeletal Radiol 1986; 15:96-102.

45. Erlemann R, Reiser MF, Peters PE, et al. Musculoskeletal neoplasms: static and dynamic Gd-DTPA--enhanced MR imaging. Radiology 1989; 171:767-773.

46. Erlemann R, Sciuk J, Bosse A, et al. Response of osteosarcoma and Ewing sarcoma to preoperative chemotherapy: assessment with dynamic and static MR imaging and skeletal scintigraphy. Radiology 1990; 175:791-796.

47. van der Woude HJ, Bloem JL, Schipper J, et al. Changes in tumor perfusion induced by chemotherapy in bone sarcomas: color Doppler flow imaging compared with contrast-enhanced MR imaging and three-phase bone scintigraphy. Radiology 1994; 191:421-431.

48. Bonnerot V, Charpentier A, Frouin F, Kalifa C, Vanel D, Di Paola R. Factor analysis of dynamic magnetic resonance imaging in

predicting the response of osteosarcoma to chemotherapy. Invest Radiol 1992; 27:847-855.

49. Fletcher BD, Hanna SL, Fairclough DL, Gronemeyer SA. Pediatric musculoskeletal tumors: use of dynamic, contrast-enhanced MR imaging to monitor response to chemotherapy. Radiology 1992; 184:243-248.

50. Hanna SL, Reddick WE, Parham DM, Gronemeyer SA, Taylor JS, Fletcher BD. Automated pixel-by-pixel mapping of dynamic contrast-enhanced MR images for evaluation of osteosarcoma response to chemotherapy: preliminary results. J Magn Reson Imaging 1993; 3:849-853.

51. van der Woude HJ, Bloem JL, Verstraete KL, Taminiau AH, Nooy MA, Hogendoorn PC. Osteosarcoma and Ewing's sarcoma after neoadjuvant chemotherapy: value of dynamic MR imaging in detecting viable tumor before surgery. AJR Am J Roentgenol 1995; 165:593-598.

52. Erlemann R. Dynamic, gadolinium-enhanced MR imaging to monitor tumor response to chemotherapy. Radiology 1993; 186:904-905.

53. Dyke JP, Panicek DM, Healey JH, et al. Osteogenic and Ewing sarcomas: estimation of necrotic fraction during induction chemotherapy with dynamic contrast-enhanced MR imaging. Radiology 2003; 228:271-278.

54. Kunisada T. Ozaki T, Kawai A, Sugihara S, Taguchi K, Inoue H. Imaging assessment of the responses of osteosarcoma patients to preoperative chemotherapy: angiography compared with thallium-201 scintigraphy. Cancer 1999; 86:949-956.

55. Ohtomo K, Terui S, Yokoyama R, et al. Thallium-201 scintigraphy to assess effect of chemotherapy in osteosarcoma. J Nucl Med 1996; 37:1444-1448.

56. Imbriaco M, Yeh SD, Yeung H, et al. Thallium-201 scintigraphy for the evaluation of tumor response to preoperative chemotherapy in patients with osteosarcoma. Cancer 1997; 80:1507-1512.

Chapter I

4-6. Figures

Fig.1 The ADC value of acetone in changing b-value from 0 to 3000 mm^{-2}.second.

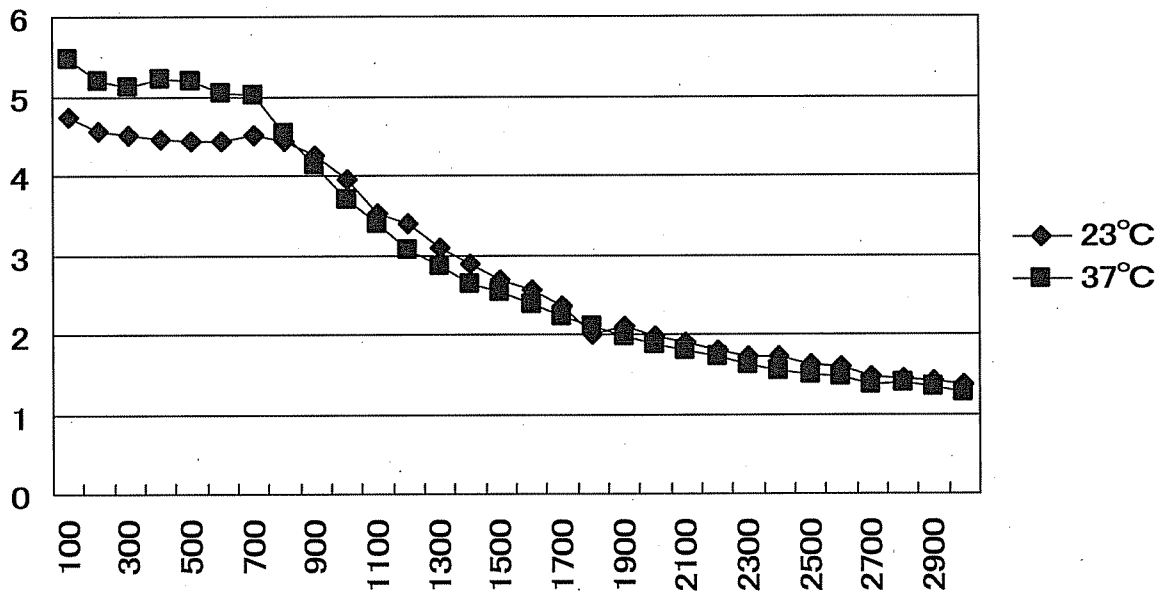

Fig 2. ADC value of DMSO in changing b-value from 0 to 3000 mm^{-2}.second.

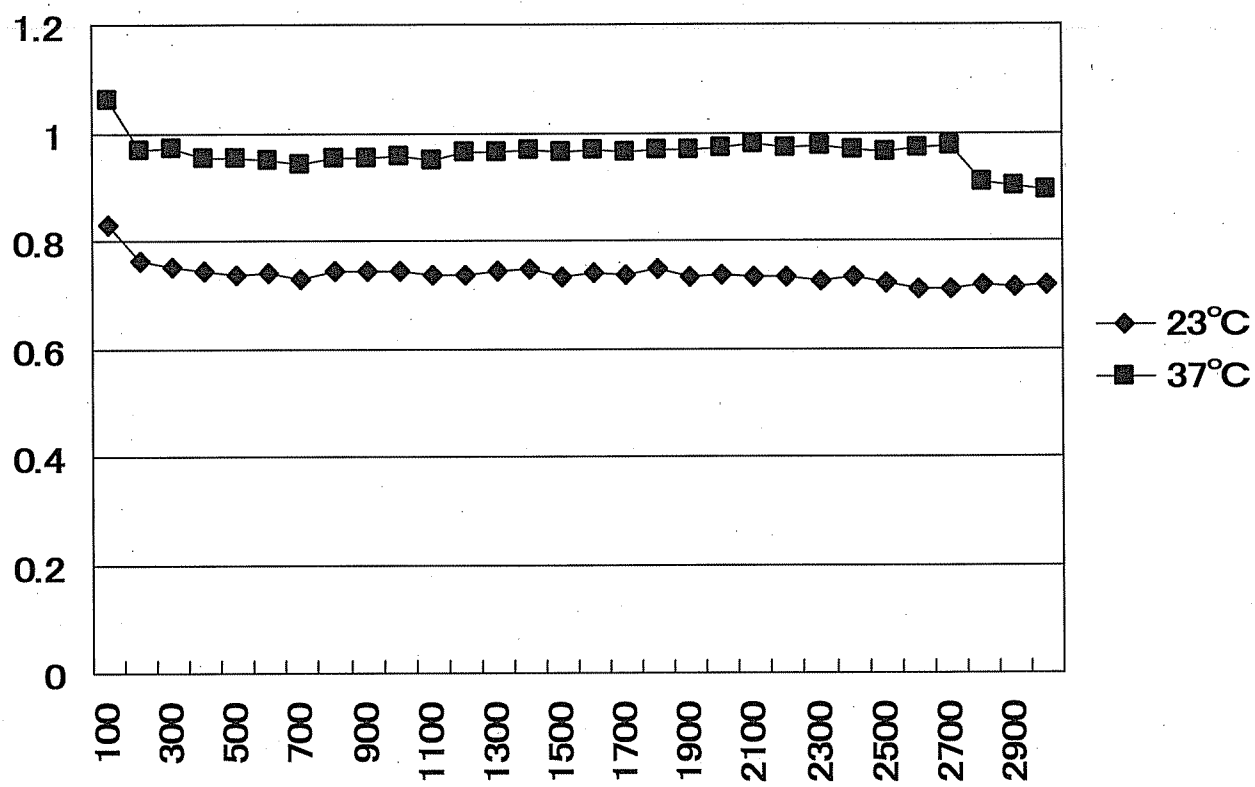

Fig 3. ADC value of water in changing b-value from 0 to 3000 mm^{-2}.second.

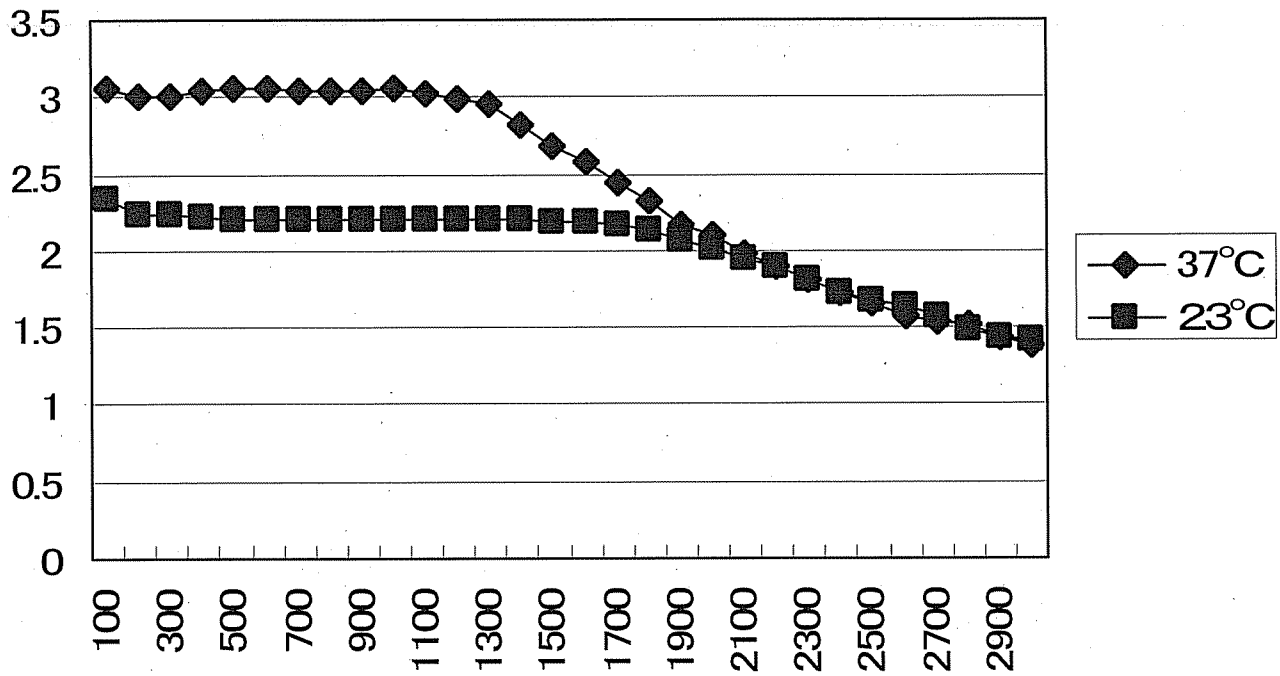

Table 1. Summary of 26 primary malignant lesions

Histopathology of primary lesion	No. of lesion	Primary site (No. of site)
Adenocarcinoma	13	
Well diff.	6	Lung (4), Ovary (1), Uterus (1)
Moderately diff.	1	Lung (1)
Poorly diff.	6	Lung (6)
Small cell ca.	3	Lung (3)
Large cell ca.	2	Lung (2)
Squamous cell ca.	2	Esophagus (2)
Papillotubular ca.	2	Breast (2)
LCNC	1	Lung (1)
Mucoepidermoid ca.	1	Lung (1)
Sarcoma	1	Synovium (1)
Malignant melanoma	1	Skin (1)

Note.- Well-diff.: well differentiated adenocarcinoma, Mederately diff.: mederately differentiated adenocarcinoma, Poorly diff.: poorly differentiated adenocarcinoma, ca.: carcinoma, LCNC: Large cell neuroendocrine carcinoma

Table 2. Summary of 13 operated brain lesions

Histopathology of brain lesion	No. of lesion	Primary site (No. of site)
Adenocarcinoma	6	
Well diff.	4	Lung (3), Ovary (1)
Poorly diff.	2	Lung (2)
Squamous cell ca.	2	Esophagus (2)
Small cell ca.	1	Lung (1)
Large cell ca.	1	Lung (1)
Papillotubular ca.	1	Breast (1)
LCNC	1	Lung (1)
Mucoepidermoid ca.	1	Lung (1)

Note.- Well diff.: well differentiated adenocarcinoma, Poorly diff.: poorly differentiated adenocarcinoma, ca.: carcinoma, LCNC: Large cell neuroendocrine carcinoma

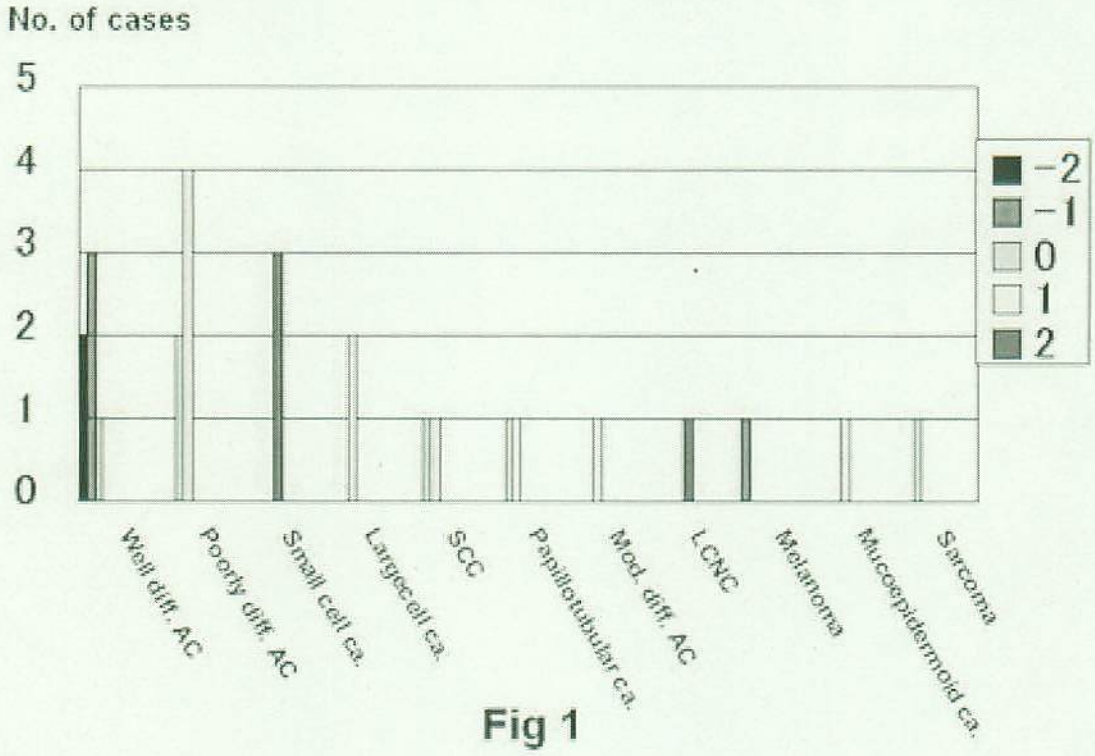

Fig 1

Chapter Ⅱ-1Fig 1. Comparison of the signal intensity of 26 metastatic brain tumors on diffusion-weighted images

All 6 well differentiated adenocarcinomas (Well diff. AC) were classified as grade -2, -1, or 0. All 3 small cell carcinomas (Small cell ca.) and 1 large cell neuroendocrine carcinoma (LCNC) were graded as +2. A malignant melanoma was grade -1; all other tumors were grade 0 or +1.

Poorly diff. AC: poorly differentiated adenocarcinomas, Large cell ca.: large cell carcinoma, SCC: squamous cell carcinoma, Papillotubular ca.: papillotubular carcinoma, Mucoepidermoid ca.: mucoepidermoid carcinoma, Mod. diff. AC: moderately differentiated adenocarcinoma,

The signal intensity was graded on 5-grade score where

-2 = hypointense relative to the normal-appearing white matter

-1 = isointense relative to the normal-appearing white matter

0 = isointense relative to the normal-appearing cortical gray matter

+1 = slightly hyperintense relative to the normal-appearing cortical gray matter

+2 = hyperintense relative to the normal-appearing cortical gray matter

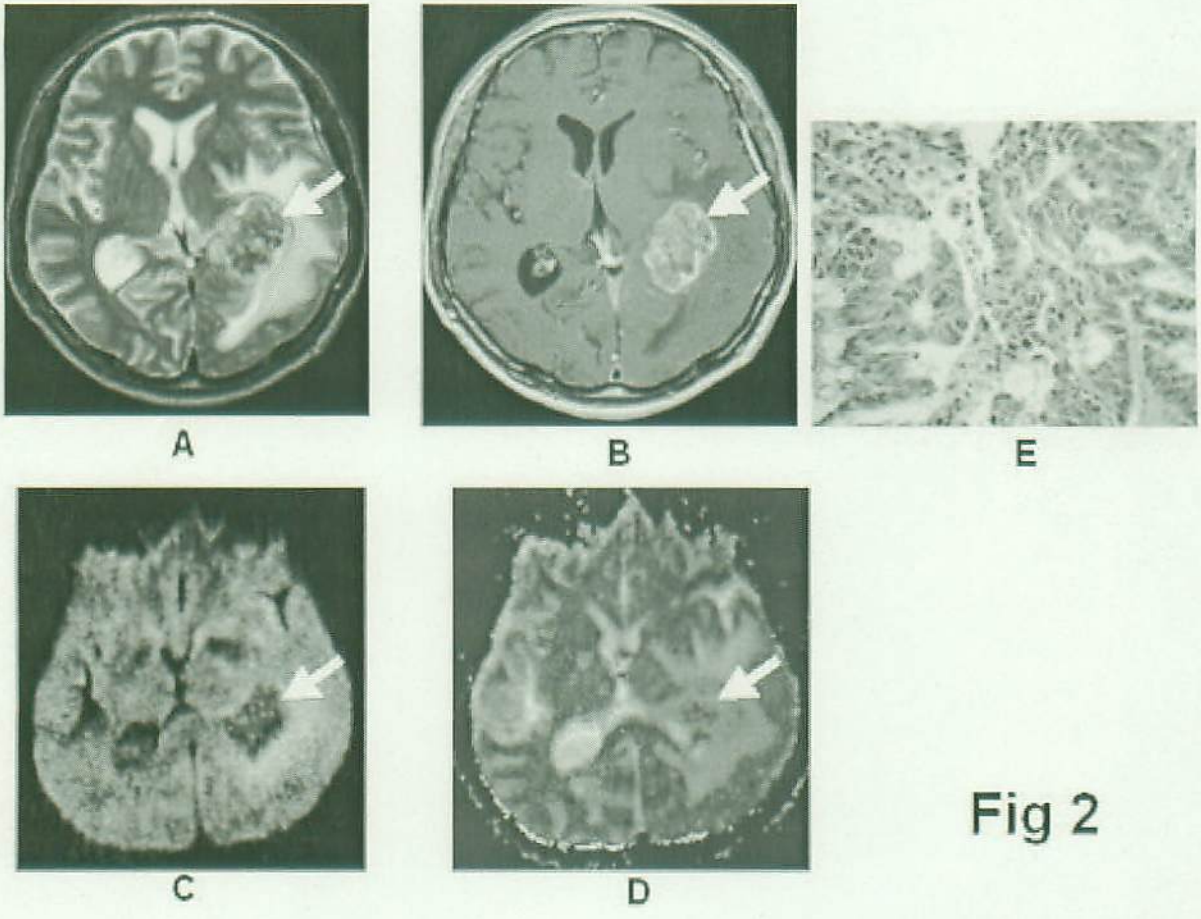

Fig 2

Chapter Ⅱ-1

Fig 2. A 67-year-old man with a well differentiated adenocarcinoma from the lung.
A. T2-weighted fast spin-echo image shows a parietotemporal lesion (arrow) near the trigone of the left lateral ventricle. It is hypointense relative to the normal-appearing white matter. The CNR of the solid lesion was 12.
B. On contract-enhanced T1-weighted image, the lesion is enhanced (arrow).
C. On DWI, the lesion is hypointense relative to the normal-appearing white matter (arrow). It was ranked as grade -2.
D. On ADC map, the nADC of the lesion was calculated as 1.95.
E. Photomicrograph of the specimen (hematoxylin-eosin stain; original magnification x 40) shows a well-differentiated acinar structure. Tumor cellularity was calculated as 0.179.

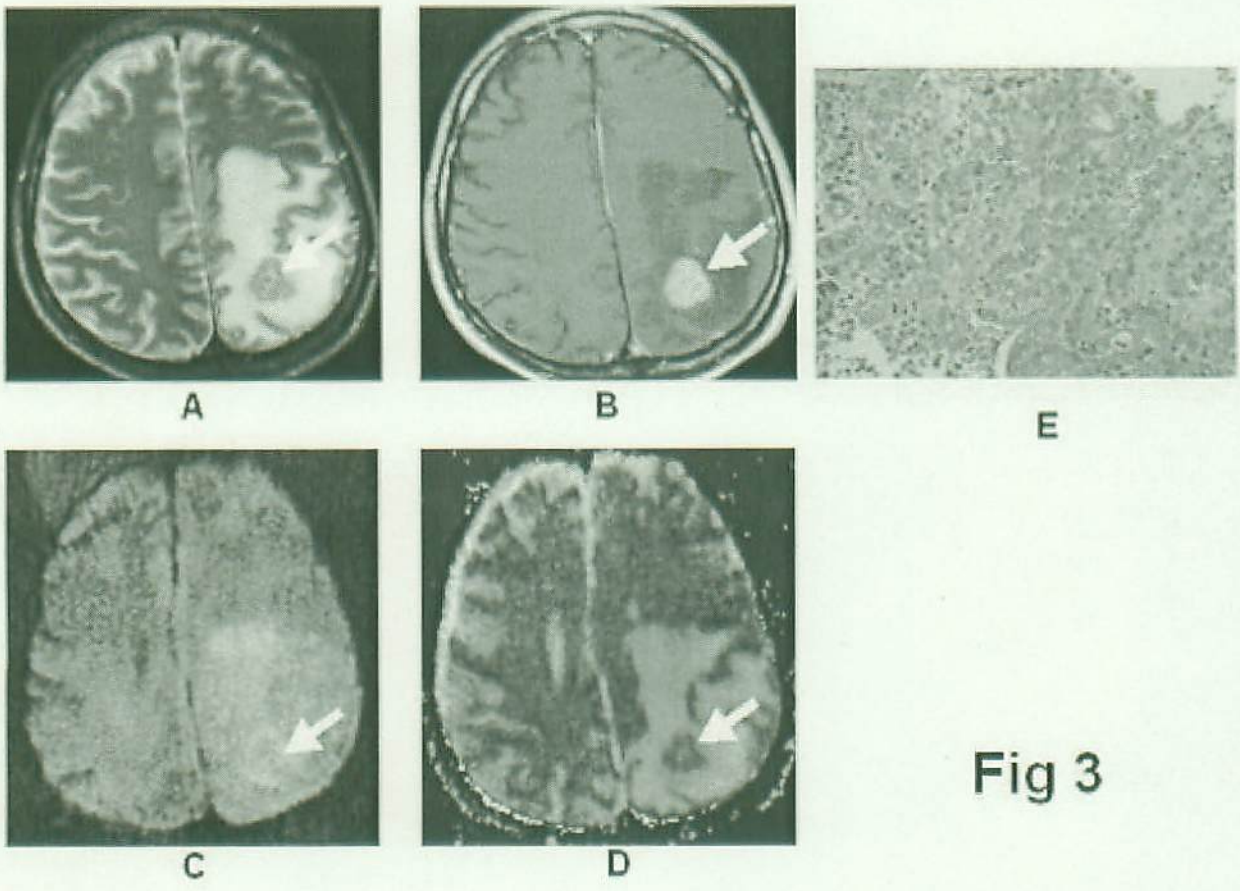

Fig 3

Chapter Ⅱ-1

Fig 3. A 41-year-old man with a poorly differentiated adenocarcinoma from the lung.

A. T2-weighted fast spin-echo image shows a left parietal subcortical lesion (arrow). It is slightly hyperintense relative to the normal-appearing white matter. The CNR of the solid lesion was 32.
B. On contract-enhanced T1-weighted image, the lesion is well enhanced (arrow).
C. On DWI, the lesion is slightly hyperintense relative to the normal-appearing cortical gray matter (arrow). It was ranked as grade +1.
D. On ADC map, the nADC of the lesion was calculated as 1.45.
E. Photomicrograph of the specimen (hematoxylin-eosin stain; original magnification x 40) shows higher cellularity than Fig 2E. Tumor cellularity was calculated as 0.334.

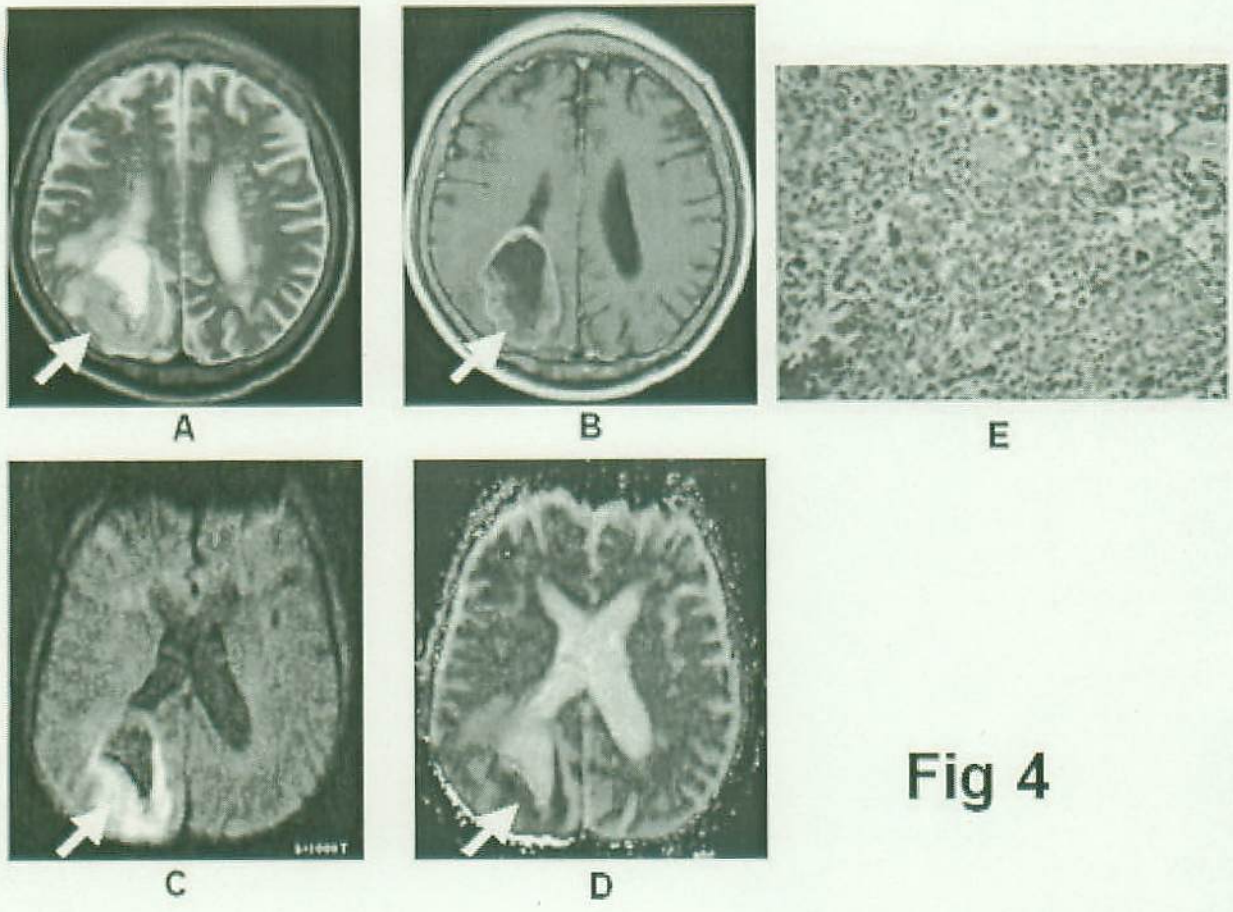

Fig 4

Chapter Ⅱ-1

Fig 4. A 69-year-old man with small cell carcinoma from the lung.

A. On T2-weighted fast spin-echo image, the solid portion of a right parietal mass lesion (arrow) is hyperintense relative to the normal-appearing white matter. The CNR of the enhancing lesion was 45.
B. On contract-enhanced T1-weighted image, the peripheral region of the lesion is enhanced (arrow).
C. On DWI, the lesion is hyperintense relative to the normal-appearing cortical gray matter (arrow). The lesion was ranked as grade +2.
D. On ADC map, the solid lesion is slightly hyperintense. Its nADC was calculated as 0.57.
E. Photomicrograph of the specimen (hematoxylin-eosin stain; original magnification x 40) shows high cellularity. The tumor cellularity was calculated as 0.72.

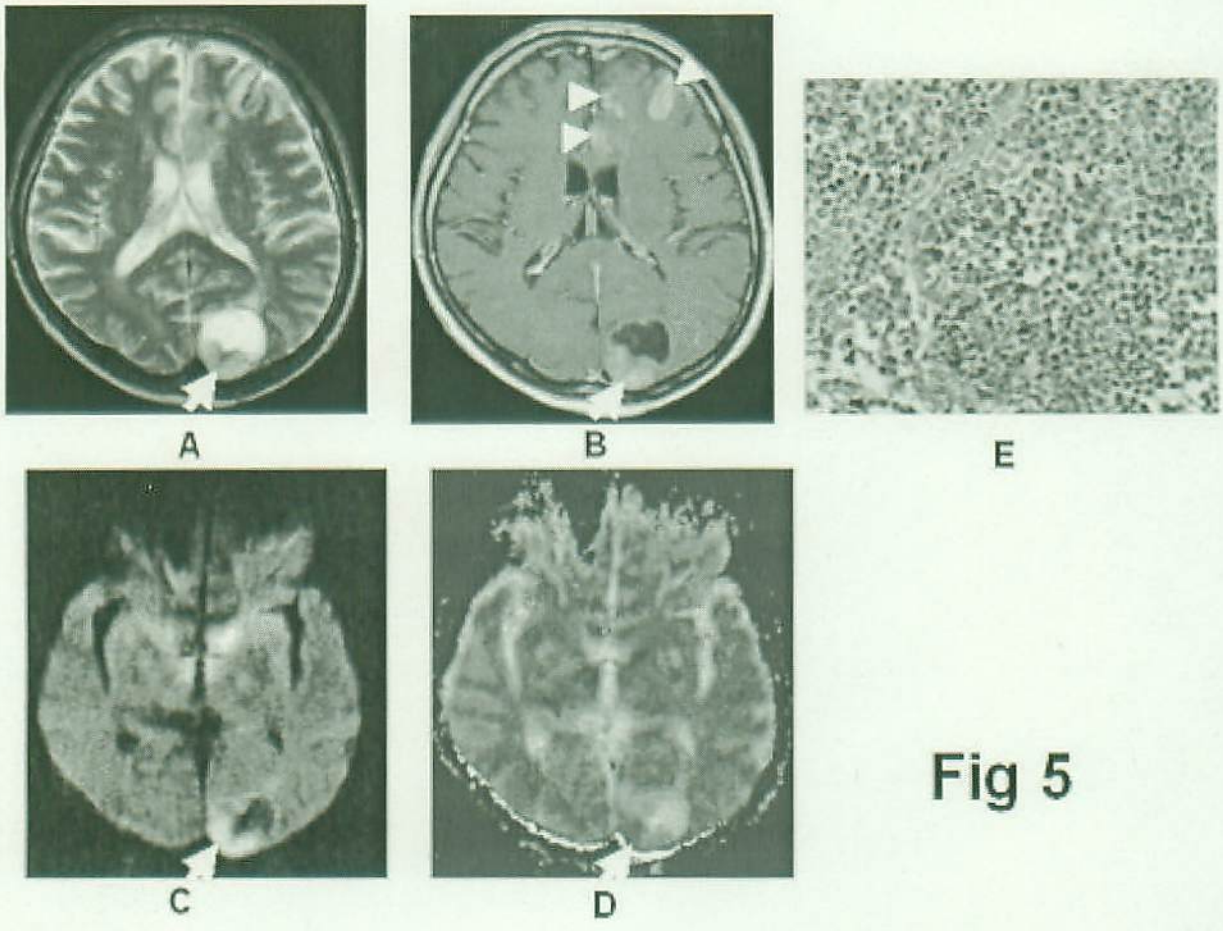

Fig 5

Chapter Ⅱ-1

Fig 5. A 63-year-old man with large cell neuroendocrine carcinoma from the lung.
A. On T2-weighted fast spin-echo image, the solid portion of left occipital lesion (arrow) is hyperintense relative to the normal-appearing white matter. The CNR of the enhancing lesion was 56.
B. On contrast-enhanced T1-weighted image, the posterior part of the lesion is enhanced (arrow). There are multiple enhancing areas (arrowheads) in the left frontal lobe indicative of subacute infarction.
C. On DWI, the solid lesion is hyperintense relative to the normal-appearing cortical gray matter (arrow). The lesion was ranked as grade +2.
D. On ADC map, the solid lesion is hypointense; its nADC was calculated as 1.04.
E. Photomicrograph of the specimen (hematoxylin-eosin stain; original magnification x 40) shows high cellularity. The tumor cellularity was calculated as 0.51.

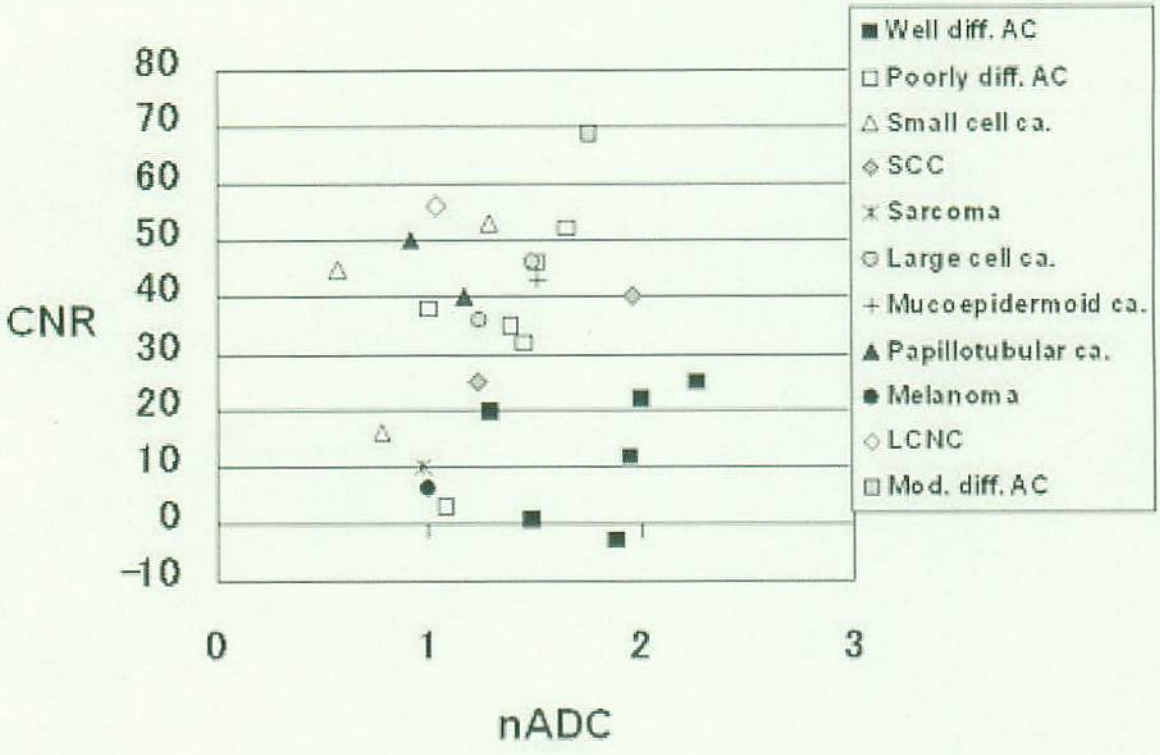

Fig 6

Chapter Ⅱ-1

Fig 6. Comparison of the nADC value and CNR on T2-weighted images of 26 metastatic brain tumors of different hystologic types.
Most well differentiated adnocarcinomas (Well diff. AC) are distributed at high nADC and low CNR. Of the 3 small cell carcinomas (Small cell ca.), 2 exhibit nADC values below 1.0. The large cell neuroendocrine carcinoma (LCNC) manifests low nADC value and high CNR. Poorly differentiated adenocarcinoma (Poorly diff. AC), papillotubular carcinoma (Papillotubular ca.), sarcoma, and malignant melanoma (Melanoma) also exhibit low nADC values.
Large cell ca.: large cell carcinoma, SCC: squamous cell carcinoma, Mucoepidermoid ca.: mucoepidermoid carcinoma, Mod. diff. AC: moderately differentiated adenocarcinoma

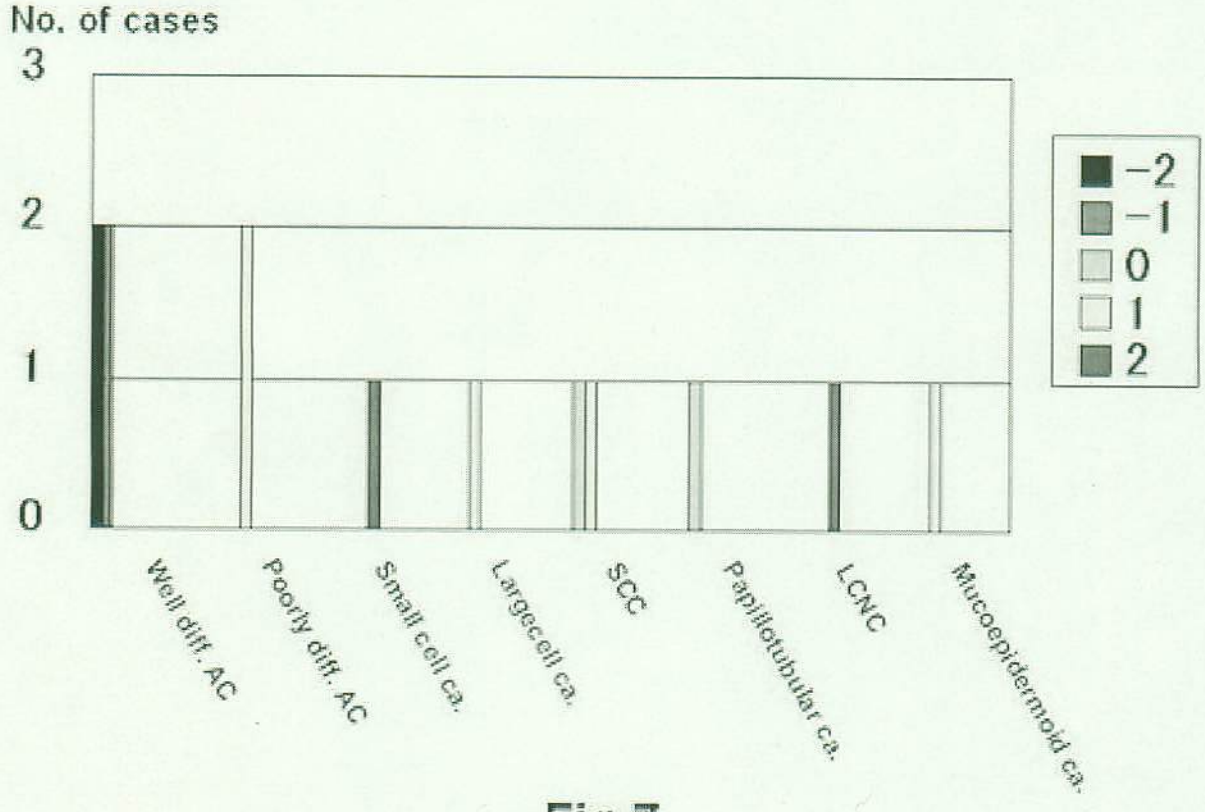

Fig 7

Chapter Ⅱ-1

Fig 7. Comparison of the signal intensity of histologically confirmed 13 brain lesions. on diffusion-weighted images
All 4 well differentiated adenocarcinomas (Well diff. AC) were graded as -2 or -1, and all 2 poorly differentiated adenocarcinomas (Poorly diff. AC) as +1. One small cell carcinoma (Small cell ca.) and one large cell neuroendocrine carcinoma (LCNC) were both graded as +2. The other lesions were graded as 0 or +1. The signal intensity was graded on 5-grade score as mentioned in Fig 1.
Large cell ca.: large cell carcinoma, SCC: squamous cell carcinoma, Papillotubular ca.: papillotubular carcinoma, Mucoepidermoid ca.: mucoepidermoid carcinoma

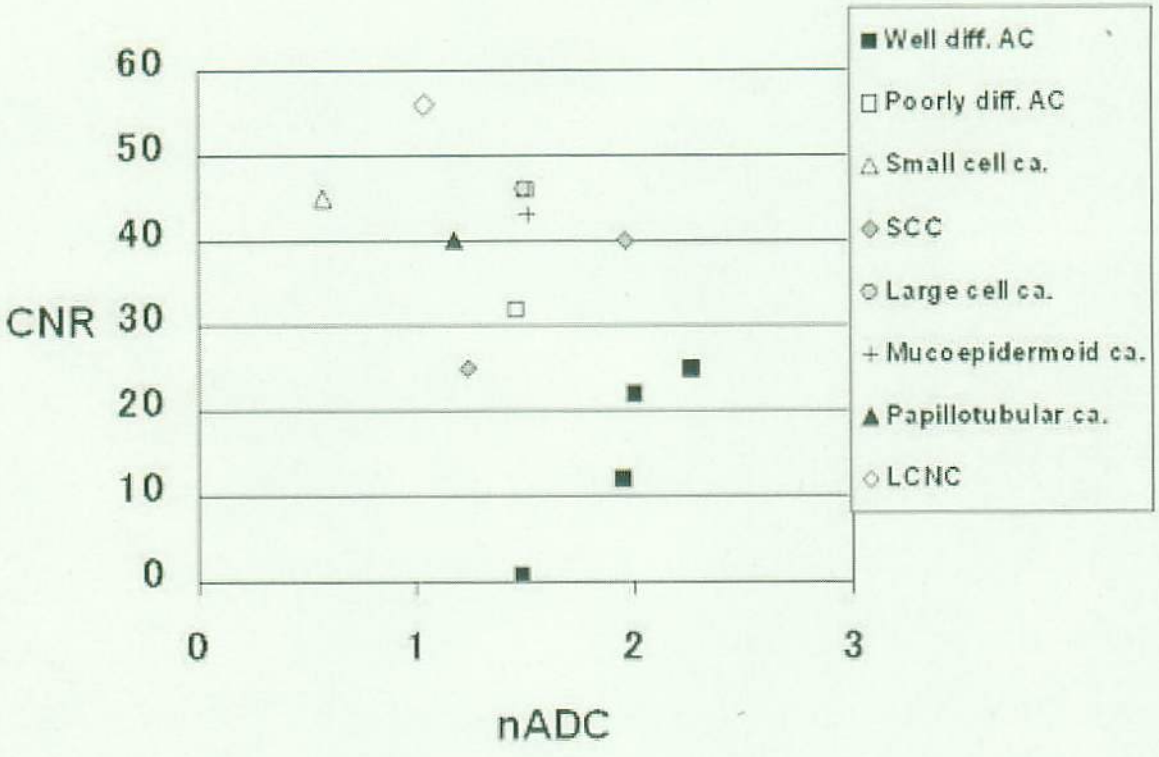

Fig 8

Chapter Ⅱ-1

Fig 8. Comparison of the nADC value and CNR on T2-weighted images of histologically confirmed 13 brain lesions.
Most well differentiated adnocarcinomas (Well diff. AC) are distributed at high nADC and low CNR. One small cell carcinomas (Small cell ca.) and one large cell neuroendocrine carcinoma (LCNC) are distributed at low nADC and high CNR. Poorly diff. AC: poorly differentiated adenocarcinoma, Large cell ca.: large cell carcinoma, SCC: squamous cell carcinoma, Mucoepidermoid ca.: mucoepidermoid carcinoma, Papillotubular ca.: papillotubular carcinoma

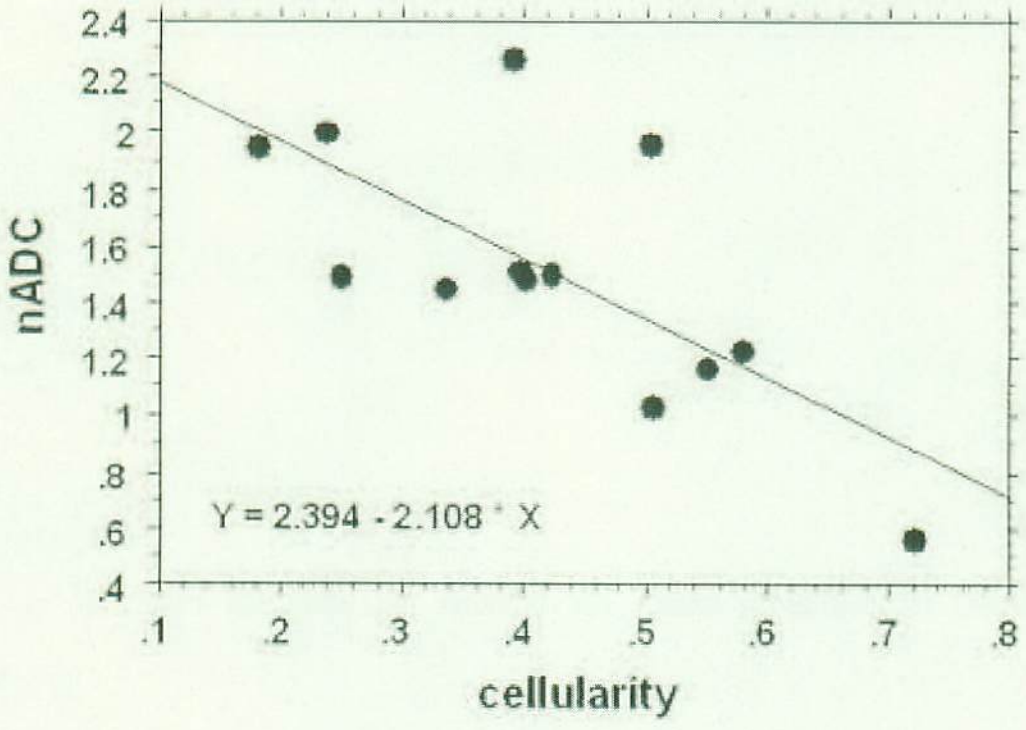

Chapter Ⅱ-1

Fig 9. Relationship between nADC and tumor cellularity.
The nADC value was inversely correlated well with tumor cellularity (r = -0.70, p = 0.0059).

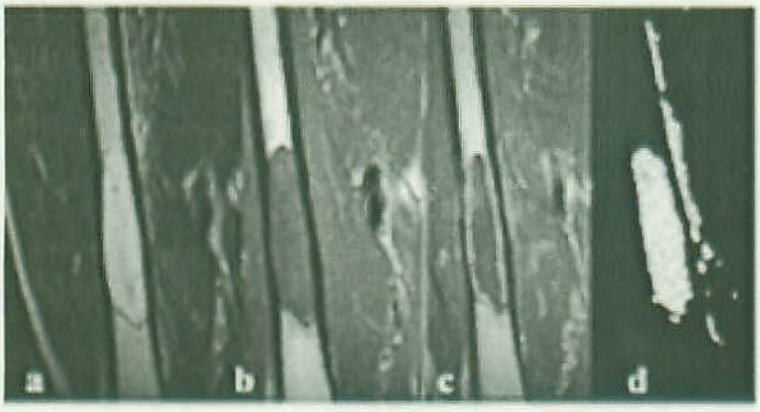

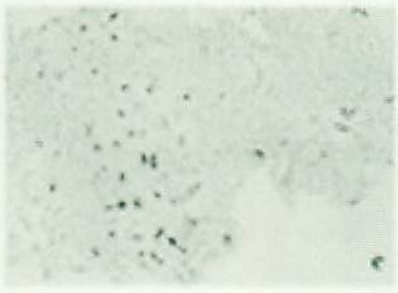

Chapter Ⅲ-1 Figure 1.

MR images and photomicrograph from a 41-year-old woman with grade 2 chondrosarcoma

a Coronal fast SE T2-weighted MRI (3500/120) showing a hyperintense mass in the right femoral bone.

b Coronal SE T1-weighted image (500/12) demonstrating a hypointense mass.

c Contrast-enhanced T1-weighted image at the same slice as in (b) showing poor enhancement in the bone mass.

d On the ADC map, the mean ADC value of this lesion is $2.3 \times 10^{-3} mm^2/s$.

e On the photomicrograph, the tumor contains cartilaginous cells with enlarged nuclei and a fine nuclear chromatin pattern (arrow). There are few cartilaginous and tumor cells in the myxoid matrix (M) (original magnification × 200; hematoxylin-eosin stain).

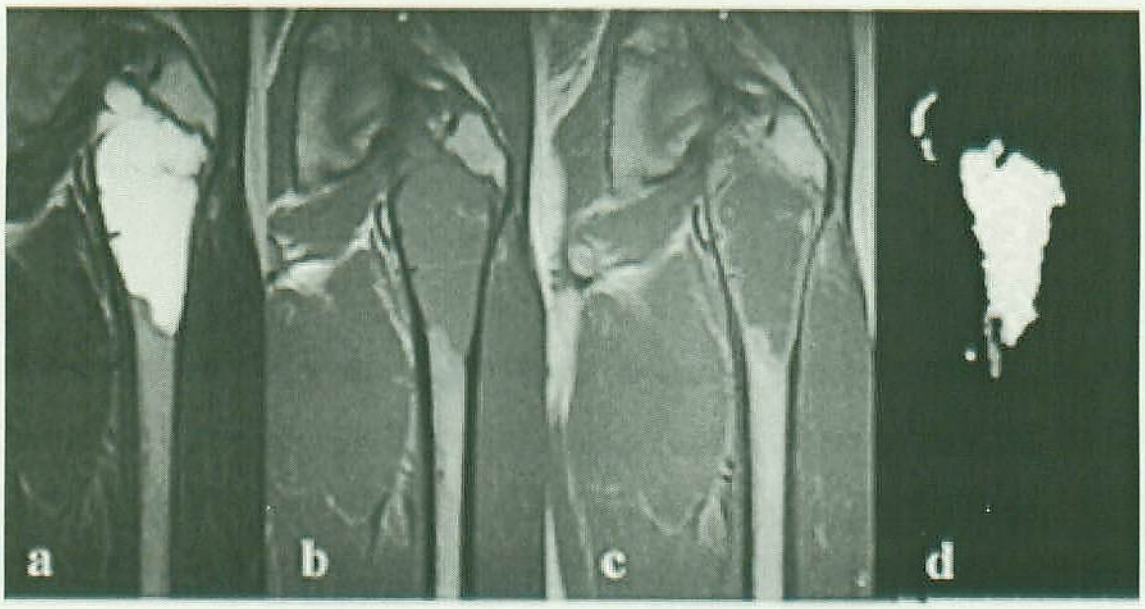

(Fig. 2 a-d)

Chapter Ⅲ-1 Figure 2.

MRI of a 17-year-old male with solitary bone cysts.

a Coronal fast SE T2-weighted MR image (3500/120) showing a lobulated hyperintense mass in the right femoral bone.

b Coronal SE T1-weighted image (500/12) demonstrating a hypointense mass.

c Contrast-enhanced T1-weighted image at the same slice as in (b) shows enhancement of the lesion wall.

d On the ADC map, the mean ADC value of this lesion is 2.67 $\times 10^{-3} mm^2/s$.

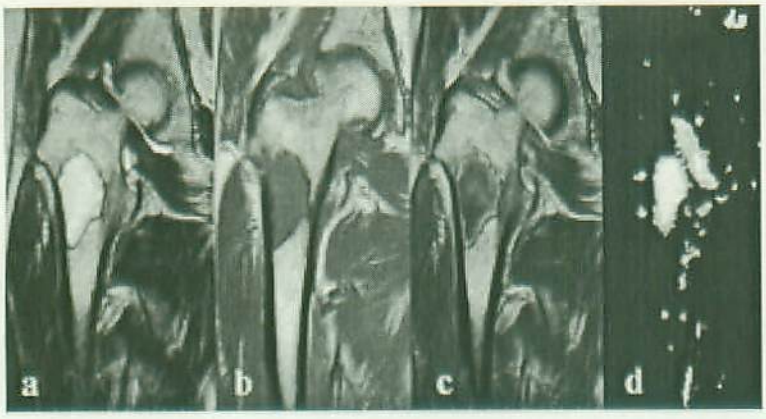

Chapter Ⅲ-1 Figure 3.

MR images and photomicrograph from a 60-year-old woman with fibrous dysplasias.

a Coronal fast SE T2-weighted MR image (3500/120) showing a hyperintense mass in the left femoral bone.

b Coronal SE T1-weighted image (500/12) demonstrating a hypointense mass.

c Contrast-enhanced T1-weighted image at the same slice as in (b) shows poor enhancement in the central portion and slight enhancement of the peripheral portion of the mass.

d On the ADC map, the mean ADC value of this lesion is $2.0 \times 10^{-3} mm^2/s$.

e The photomicrograph shows absorbed woven bones (WB) and very thin, fibrous tissues (F) (original magnification ×100; hematoxylin-eosin stain).

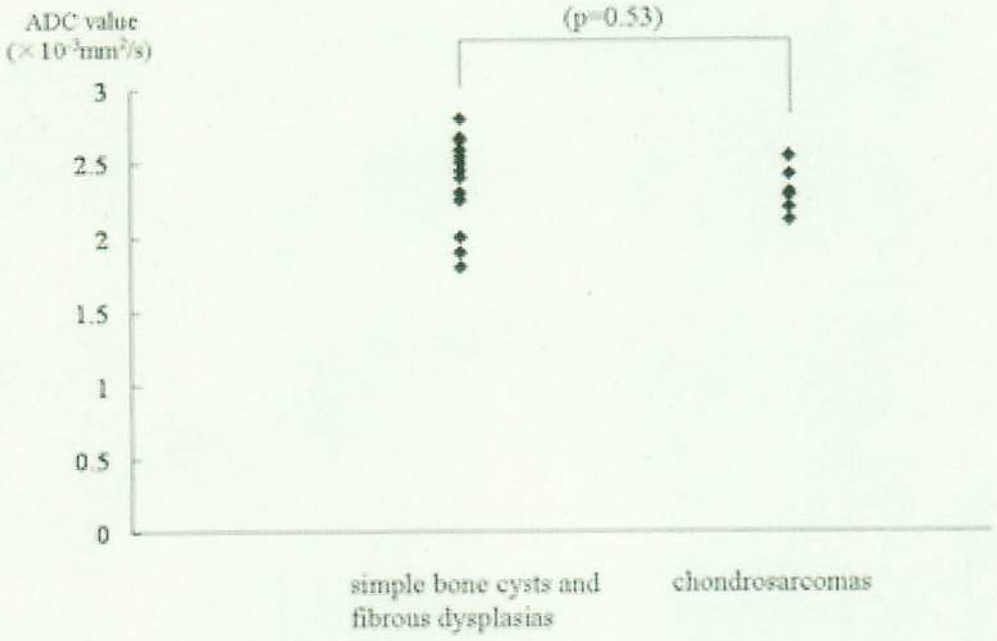

(Fig 4)

Chapter Ⅲ-1 Figure 4.

Comparison of the ADC value between 2 types of benign lesions (solitary bone cysts and fibrous dysplasias) and chondrosarcomas. The mean ADC values of chondrosarcomas and 2 benign lesions are $2.29 \pm 0.21 \times 10^{-3} mm^2/s$ and $2.37 \pm 0.31 \times 10^{-3} mm^2/s$, respectively. There is no statistical difference between 2 types of benign lesions and chondrosarcomas (p=0.53).

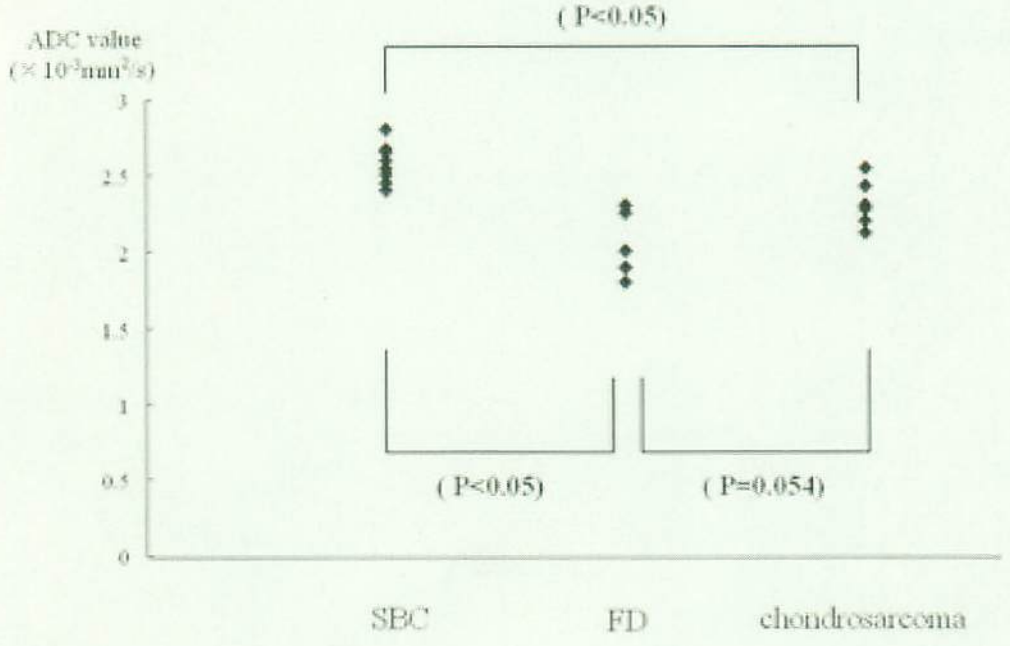

(Fig 5)

Chapter Ⅲ-1 Figure 5.

Comparison of the ADC values among solitary bone cysts, fibrous dysplasias, and chondrosarcomas. The mean ADC value of simple bone cysts ($2.57 \pm 0.13\times10^{-3}$ mm^2/s) is significantly higher than that of fibrous dysplasias and chondrosarcomas ($2.0 \pm 0.21\times10^{-3}$ mm^2/s and $2.29 \pm 0.14\times10^{-3}$ mm^2/s, $p<0.05$). The mean ADC value of chondrosarcomas is higher than that of fibrous dysplasias, however, the difference is not statistically significant ($p=0.054$)

Fig. 1

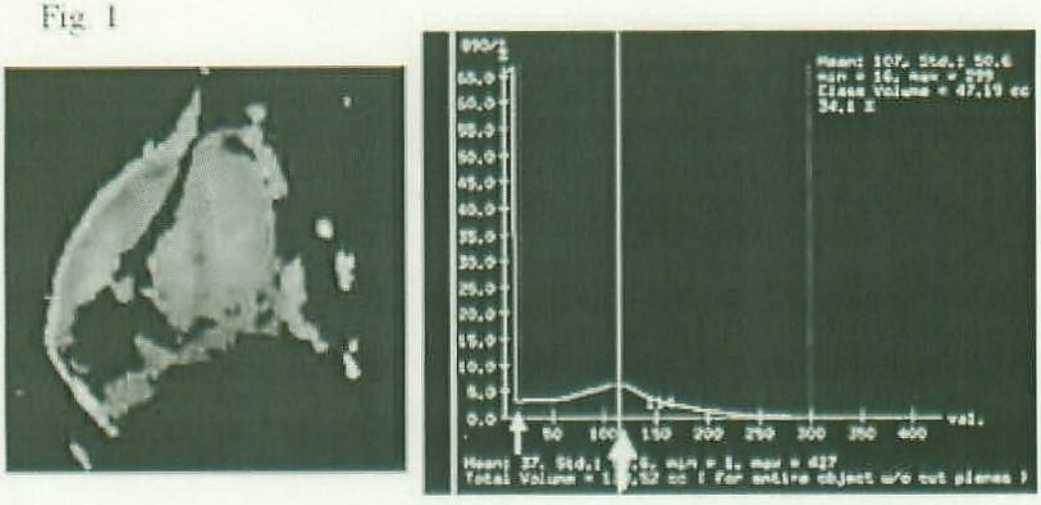

(a) (b)

Chapter Ⅲ-2 Figure 1

(a) ADC map of the left femoral bone in 14-year-old female with osteosarcoma (same patient as in Fig.5). Note that normal bone marrow, ossification in the sarcoma and cortex of the femoral bone shows no signal intensity. The bone marrow contains rich fat, and the cortex of the bone and the ossification in the sarcoma is rich in minerals. Because we used the fat suppression technique in DWI, the ADC value of normal bone marrow was 0×10^{-3} mm^2/sec. As areas rich in minerals contain no proton molecules, they usually emit a null signal on the MRI image and their ADC value tends to be 0×10^{-3} mm^2/sec.

(b) Histogram of 5-slice tumor images of ADC maps in a 14-year-old female with osteosarcoma (same patient as in Fig. 5). To avoid voxels with an ADC value of 0, 5-slice tumor images from the ADC map were transferred to a workstation and histogram analysis was performed to determine the mean ADC value of the voxels containing pre- and post-treatment tumor tissue (large arrow), cutting off voxels with a value of 0 (small arrow).

Fig. 2 Change of ADC value before and after therapy

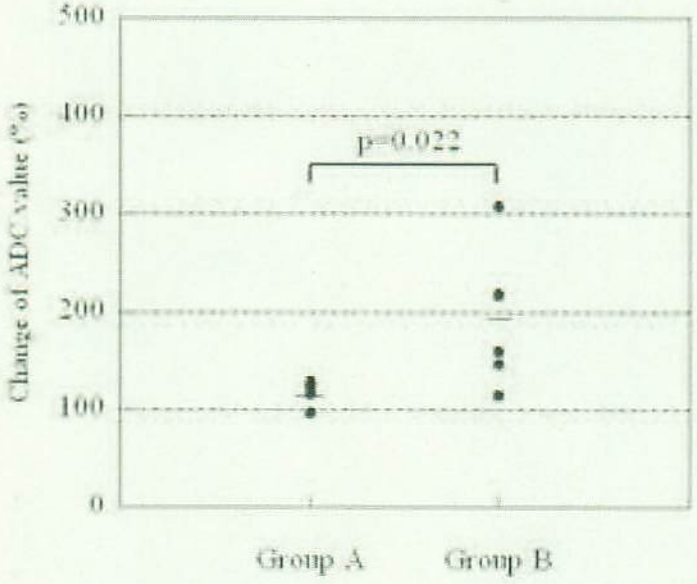

Chapter Ⅲ-2 Figure 2

Graph comparing the changes in the ADC value before and after therapy in groups A and B. The post-treatment ADC values were significantly higher in group B than group A (p=0.001). Short horizontal bars indicate the mean of each group.

Fig. 3 Change of tumor T2-CNR before and after therapy

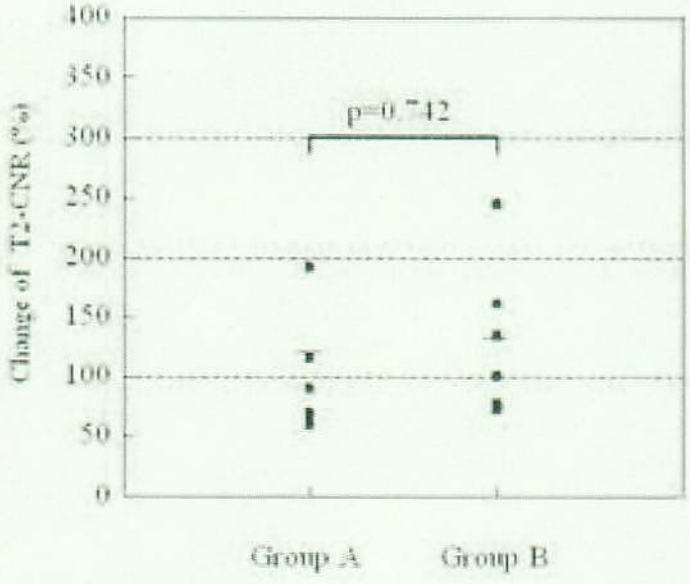

Chapter Ⅲ-2 Figure. 3

Graph comparing the changes in the CNR on T2-weighted images obtained before and after therapy in groups A and group B. There was no significant difference between the 2 groups (p=0.849). Short horizontal bars indicate the mean of each group.

Fig 4 Change of tumor volume before and after therapy

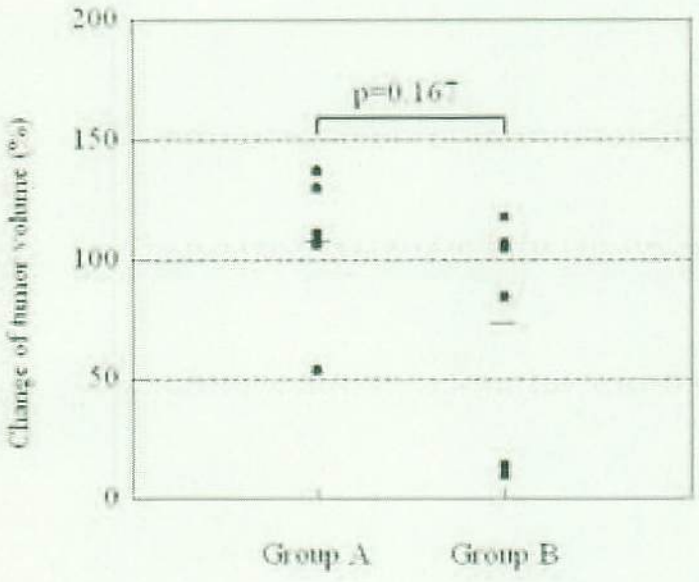

Chapter Ⅲ-2 Figure 4

Graph comparing the changes in the tumor volume before and after therapy in groups A and B. There was no significant difference between the 2 groups (p=0.078). Short horizontal bars indicate the mean of each group.

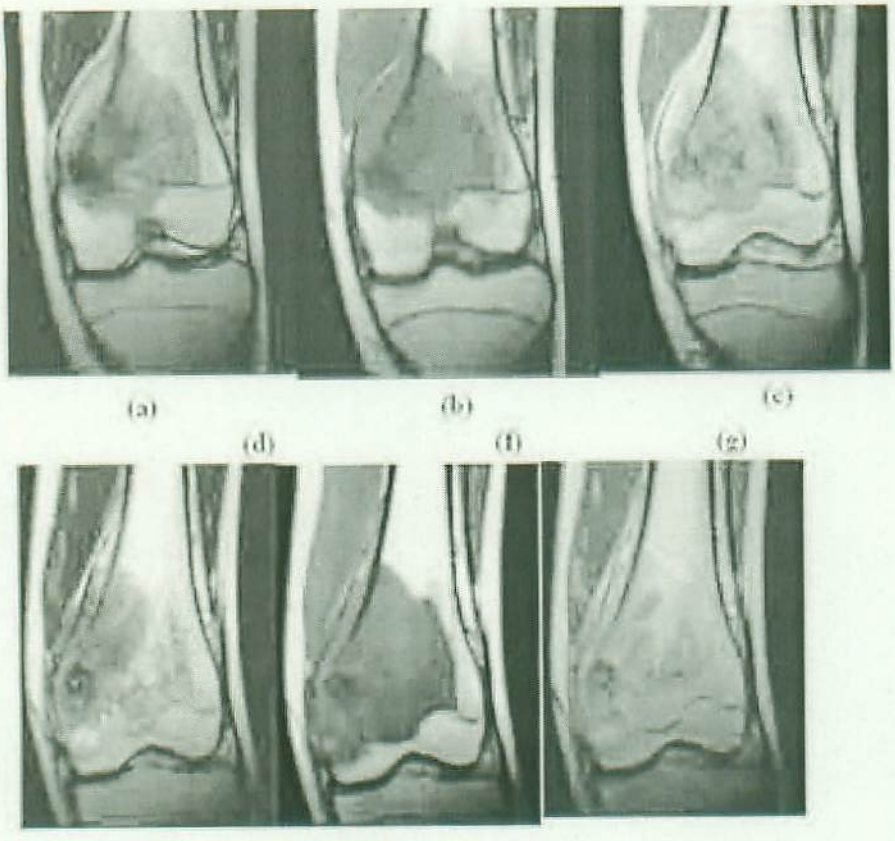

Fig. 5

Chapter Ⅲ-2 Figure 5

Osteosarcoma in a 14-year-old female

T2- (a), T1- (b), and Gd-enhanced T1-weighted image (c) before chemotherapy and T2- (d), T1- (e), and Gd-enhanced T1-weighted image (f) after chemotherapy. After chemotherapy, the tumor showed slightly higher signal intensity on the T2-weighted image. However, its size was increased and it was enhanced homogeneously after the injection of gadolinium. The mean ADC value increased from 1.07 to 1.3 x 10^{-3} mm^2/sec after therapy. After the operation, the necrotic area of this tumor exceeded 90%.

Tables

Case No.	Pathological Diagnosis	Location	Treatment	Percent of tumor necrosis after chemo-or radiotherepy
1	osteosarcoma	lt. femoral bone	chemotherapy+operation	60
2	osteosarcoma	rt. femoral bone	chemotherapy+operation	70
3	osteosarcoma	lt. femoral bone	chemotherapy+operation	90
4	osteosarcoma	rt. femoral bone	chemotherapy+operation	50
5	osteosarcoma	rt. femoral bone	chemotherapy+operation	95
6	osteosarcoma	lt. femoral bone	chemotherapy+operation	60
7	osteosarcoma	rt. femoral bone	chemotherapy+operation	70
8	osteosarcoma	rt. humeral bone	chemotherapy+operation	55
9	osteosarcoma	lt. femoral bone	chemotherapy+operation	25
10	osteosarcoma	lt.tibial bone	chemotherapy+operation	95
11	osteosarcoma	rt.femoral bone	chemotherapy+operation	90
12	Ewing sarcoma	lt. fibral bone	chemotherapy+operation	90
13	Ewing sarcoma*	rt. femoral bone	radiation	-
14	Ewing sarcoma*	pelvis bone	radiation	-

Chapter Ⅲ-2 Table 1 Clinical data of 14 primary bone tumors and the percentage of tumor necrosis or degeneration after total tumor excision.

Note. * There is no macroscopic regrowth of the tumor 2.5 years after the first chemotherapy.

Group	Case No.	ADC value		
		Before theraphy (a)	After therapy (b)	b/a (%)
A	1	1.07	1.35	126
A	2	1.30	1.47	113
A	4	1.90	2.30	121
A	6	2.00	2.30	115
A	7	1.24	1.40	113
A	8	1.18	1.10	93
A	9	1.00	1.15	115
B	3	0.77	1.11	144
B	5	1.38	2.17	157
B	10	1.10	1.98	180
B	11	1.00	1.90	190
B	12	0.63	1.96	311
B	13	1.10	2.40	218
B	14	1.06	2.30	217

Chapter III-2 Table 2: The changes in the ADC value in the 14 bone tumors in group A and B before and after treatment.

Note. SD=standard deviation.

Group	Case No.	T2-CNR		
		Before theraphy (a)	After therapy (b)	b/a (%)
A	1	5.39	10.42	193
A	2	5.39	10.40	193
A	4	3.32	3.89	117
A	6	19.80	18.00	91
A	7	13.30	13.50	102
A	8	9.50	5.72	60
A	9	16.40	11.30	69
B	3	2.97	4.00	135
B	5	5.53	4.10	74
B	10	13.80	10.4	75
B	11	14.40	14.10	98
B	12	11.70	9.10	78
B	13	4.63	11.40	246
B	14	4.56	7.40	162

Chapter Ⅲ-2 Table 3: The changes in CNR on T2WI in the 14 bone tumors in group A and B before and after treatment.

Abbreviation. CNR= contrast noise ratio T2WI=T2 weighted image

Group	Case No.	tumor volume		
		Before theraphy (a)	After therapy (b)	b/a (%)
A	1	89.3	94.5	106
A	2	148.2	202.9	137
A	4	165.9	215.0	130
A	6	28.2	30.4	108
A	7	31.0	92.5	298
A	8	33.9	149.1	440
A	9	32.3	17.3	54
B	3	58.3	68.6	118
B	5	125.0	106.4	85
B	10	18.6	21.0	113
B	11	40.0	35.1	88
B	12	965.2	139.8	14
B	13	146.4	156.4	107
B	14	696.5	67.0	10

Chapter III-2 Table 4: The changes in the tumor volume in the 14 bone tumors in group A and B before and after treatment.